

# M<sup>3</sup>Depth: Wavelet-Enhanced Depth Estimation on Mars via Mutual Boosting of Dual-Modal Data

Junjie Li, *Graduate Student Member, IEEE*, Jiawei Wang, *Graduate Student Member, IEEE*, Miyu Li, Yu Liu, *Member, IEEE*, Yumei Wang, *Member, IEEE*, and Haitao Xu

**Abstract**—Depth estimation plays a great potential role in obstacle avoidance and navigation for further Mars exploration missions. Compared to traditional stereo matching, learning-based stereo depth estimation provides a data-driven approach to infer dense and precise depth maps from stereo image pairs. However, these methods always suffer performance degradation in environments with sparse textures and lacking geometric constraints, such as the unstructured terrain of Mars. To address these challenges, we propose M<sup>3</sup>Depth, a depth estimation model tailored for Mars rovers. Considering the sparse and smooth texture of Martian terrain, which is primarily composed of low-frequency features, our model incorporates a convolutional kernel based on wavelet transform that effectively captures low-frequency response and expands the receptive field. Additionally, we introduce a consistency loss that explicitly models the complementary relationship between depth map and surface normal map, utilizing the surface normal as a geometric constraint to enhance the accuracy of depth estimation. Besides, a pixel-wise refinement module with mutual boosting mechanism is designed to iteratively refine both depth and surface normal predictions. Experimental results on synthetic Mars datasets with depth annotations show that M<sup>3</sup>Depth achieves a significant 16% improvement in depth estimation accuracy compared to other state-of-the-art methods in depth estimation. Furthermore, the model demonstrates strong applicability in real-world Martian scenarios, offering a promising solution for future Mars exploration missions.

**Index Terms**—Mars rover, 3D scene perception, depth estimation, stereo matching, multi-modal.

## I. INTRODUCTION

LIMITED scene perception capabilities have become a critical bottleneck in the traveling speed of current Mars rovers [1], which hinders the efficient completion of scientific tasks. For example, the Curiosity Rover encounters delays and slowdowns when navigating around obstacles like rocks, resulting in an average travel distance of only 28.9 meters per sol [2]. Similarly, the Zhurong Rover covers merely 6.2

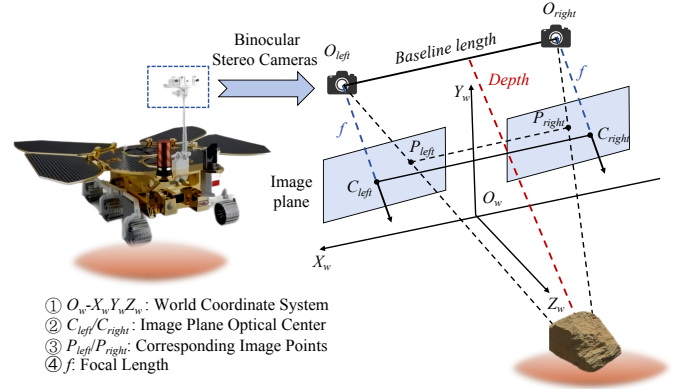


Fig. 1. An illustration of China Zhurong Rover stereo camera. Given the focal length and baseline length of the camera, the depth can be calculated by calculating the pixel horizontal difference (*i.e.* disparity) of image points in the left and right imaging planes.

meters per sol [3]. Depth estimation holds great potential for enhancing scene perception. It provides a more comprehensive understanding of the 3D structure [4] compared to 2D approaches, such as terrain categorization [5] and semantic segmentation [6]. Therefore, 3D perception abilities are essential to support further Martian scientific tasks, as they enable critical operations such as robotic navigation and obstacle avoidance [7].

Depth information not only enhances navigation capabilities of Mars rovers but also complements traditional downstream 2D vision tasks. As demonstrated in [8], the white trapezoid-shaped marker on the Curiosity Rover serves as a scale bar to roughly estimate depth and further refines the distinction between bedrock and rock categorization. Studies, such as those in [6], [9], [10], have shown that integrating depth information as auxiliary input can significantly improve semantic segmentation precision. Therefore, it is crucial to investigate stereo depth estimation to improve both the 3D scene perception capabilities of Mars rovers and optimize traditional 2D vision tasks.

Depth estimation from RGB images has long been explored by the computer vision community. However, this problem is fundamentally ill-posed due to the inherent ambiguity of projecting 3D scenes onto 2D images. One common approach used to tackle this issue is stereo matching, which determines disparity by aligning similar pixel features between rectified left and right image pairs. Mars rovers such as China's Zhurong Rover [11] and NASA's Perseverance Rover [12], are both equipped with stereo cameras. Leveraging principles

This work was supported in part by the National Key Research and Development Program of China under Grant 2022YFB2902705, in part by Beijing University of Posts and Telecommunications (BUPT) Excellent Ph.D. Students Foundation under Grant CX20241090, and in part by BUPT Innovation and Entrepreneurship Support Program under Grant 2025-YC-T025. *Corresponding author: Yu Liu* (e-mail: liuy@bupt.edu.cn).

J. Li, M. Li, Y. Liu, and Y. Wang are with the School of Artificial Intelligence, Beijing University of Posts and Telecommunications, Beijing 100876, China (e-mail: junjie@bupt.edu.cn; miyuli@bupt.edu.cn; ymwang@bupt.edu.cn).

J. Wang is with State Key Laboratory of Networking and Switching Technology, Beijing University of Posts and Telecommunications, Beijing 100876, China (e-mail: wangjiawei98@bupt.edu.cn).

H. Xu is with National Space Science Center, Chinese Academy of Sciences, Beijing 100190, China (e-mail: xuhaitao@nssc.ac.cn)

of computational photography, these stereo cameras unlock the potential for depth estimation from captured stereo image pairs. As depicted in Fig. 1, with the camera focal length and baseline length provided, the horizontal difference in pixel location (*i.e.* disparity) can be converted into depth based on the geometric principles of parallel binocular vision.

Mars presents an unstructured environment dominated by smooth, texture-less surfaces and a lack of prominent edges [13]–[15], which are primarily composed of low-frequency signals. Conventional learning-based stereo depth methods struggle to extract meaningful features due to the absence of distinguishable textures when applied in Mars. At the same time, existing neural network architectures exhibit a notable bias toward high-frequency features, as analyzed in [16], [17]. This bias means that current networks often prioritize sharp and distinct details while being prone to neglecting low-frequency information, further exacerbating the difficulty of feature extraction in the Martian environment.

Traditional stereo matching methods primarily focus on matching pixels across two images captured from slightly different viewpoints, while heavily relying on manual feature descriptors [18], [19]. With the rapid advancements in deep learning, stereo depth estimation methods have witnessed an explosion in accuracy and inference speed [20]. By utilizing the architectural topology of neural networks, these models establish an effective mapping between the input data and corresponding depth labels in an end-to-end manner, eliminating the reliance on manual feature design [21], [22]. Despite these advancements, these models highly depend on distinctive textures for feature extraction, limiting their performance in environments with sparse or ambiguous visual features. Furthermore, relying solely on feature matching constraint between image pairs proves insufficient for precise correspondence estimation [23]. Without explicit geometric constraints (such as epipolar geometry [24] and planar assumptions [25]), these models often fail to capture the intricate three-dimensional structures of the scene, leading to suboptimal depth predictions. **Surface normal map**, as another modality, is visually discriminative and geometrically informative, offering localized geometric properties compared to the broader geometric attributes of depth [26]. Additionally, surface normal maps are much easier to interpret visually and exhibit scale-invariance [4]. In contrast, many existing geometric constraints, such as epipolar geometry and planar assumptions, rely on structured surfaces, strong texture cues, or large-scale training datasets to function effectively [27]. Most importantly, as a critical 3D representation form, surface normal map and depth exhibit a strong geometric relationship and are highly complementary [28], which makes it feasible to leverage the surface normal as a constraint to enhance Martian depth estimation accuracy.

To summarize, due to Martian unique terrain characteristics, accurate depth estimation on Mars is non-trivial. To address this, two fundamental issues must be considered: 1) *How to eliminate the issues of many neural networks neglecting low-frequency features, which hampers performance in Mar’s low-texture, unstructured terrain*, and 2) *How to leverage surface normals as explicit geometric constraints to enhance*

*the model’s ability to capture global spatial relationships and achieve more accurate depth estimation*. Considering above issues, we aim to emphasize the importance of low-frequency signals by considering the frequency domain characteristics of Martian terrains. Additionally, we exploit the use of surface normal map as an auxiliary modality, leveraging their complementary geometric information to enhance the precision of depth estimation. Specifically, we propose M<sup>3</sup>Depth, a wavelet-enhanced Depth estimation model on Mars via Mutual boosting of dual-Modal data, as detailed in Fig. 5. Considering the dominance of low-frequency components and the lack of high-frequency features in Martian stereo images, we introduce a wavelet-enhanced convolutional kernel to better retain the low-frequency components, while expanding the receptive field size to capture global scene context more effectively. Moreover, we incorporate the surface normal as a geometric constraint and introduce a consistency loss to explicitly model the inherent geometric relationship between depth map and surface normal map. To further improve the accuracy of depth estimation, we develop a pixel-wise refinement module that iteratively enhances both depth and surface normal predictions through a mutual-boosting mechanism.

In summary, the key contributions of our work are as follows.

- 1) We propose a learning-based stereo depth estimation model tailored for Mars rovers, designed to address the unique challenges posed by Martian unstructured environment.
- 2) We utilize a learnable wavelet frequency domain feature extraction module that effectively preserves critical low-frequency information in Martian stereo images while simultaneously expanding the receptive field size.
- 3) We introduce a consistency loss to regularize the geometric relationship between depth maps and surface normal maps. In addition, we employ an iterative refinement module to enable mutual boosting between depth and surface normal, achieving more accurate and continuous predictions.
- 4) We perform comprehensive evaluations on a synthetic Mars dataset, demonstrating significant improvements in depth estimation accuracy. Besides, we evaluate its adaptability and generalization on real Martian images.

The remainder of this paper is organized as follows. Section II surveys existing research on stereo depth estimation. Section III presents the proposed framework for depth estimation, while Section IV details the designed methods and modules. Experimental configurations and results are demonstrated in Section V. Finally, the conclusions are summarized in Section VI.

## II. RELATED WORK

In this section, we review the current works and discuss the key ideas that have inspired the design of our approach.

### A. Mars Scene Perception

Datasets form the cornerstone for Mars scene perception tasks. Among the earliest efforts, Ai4Mars [8] introduced



a Mars terrain segmentation dataset based on images from the Curiosity Rover, focusing on semantic segmentation of Martian surfaces. Subsequently, Zhang *et al.* [29] released the S<sup>5</sup>Mars dataset, better addressing the challenges of identifying complex terrains. Based on China TianWen-1 mission, Lv *et al.* [30] introduced the first Mars rock segmentation dataset leveraging images from the Zhurong Rover. To mitigate the scarcity of high-quality real-world data, Ma *et al.* [10] generated highly realistic synthetic datasets, thus expanding the data resources available for Martian scene perception tasks.

As for Martian scene perception tasks, they can be broadly categorized into 2D (e.g. terrain classification [5] and semantic segmentation [6], [9], [10], [29], [30]) and 3D perspectives (e.g. stereo-based distance measurement [31] and scene reconstruction [32]). In terrain classification, Panambur *et al.* [5] proposed a self-supervised method to cluster sedimentary textures, enabling the classification of Martian surface materials. Beyond terrain classification, semantic segmentation has been a predominant task to classify the Martian surface into different categories. Such segmentation techniques [6], [9], [10], [29], [30] help differentiate between various terrain types, focusing primarily on pixel-level labels. However, above approaches focused mainly on 2D texture or category analysis are inherently limited, as they fail to fully capture the three-dimensional structure of the environment. To address this, researchers have also explored 3D scene reconstruction techniques. Zheng *et al.* [31] enhanced stereo matching algorithms for Mars images, enabling a rough estimation of rock distances, while Liu *et al.* [32] utilized seamless stitching methods to integrate individual block models into a unified coordinate system, producing spatially continuous 3D scene models. Despite these advancements, existing 3D approaches generally offer only coarse geometric information. This highlights the need for refined depth estimation techniques, which can yield more accurate and comprehensive 3D representations of Martian terrains.

### B. Stereo Depth Estimation

Building on the success of deep learning, traditional stereo matching [33], [34] have been largely surpassed by learning-based approaches [35]–[37], significantly enhancing stereo vision system performance. Modern CNN-based stereo depth estimation methods effectively handle complex real-world scenes by extracting pixel-wise features in an end-to-end manner [38]–[40]. These methods mostly construct a cost volume by computing matching scores between stereo image pairs, which is then refined by high-level networks to estimate disparities.

However, stereo depth estimation still remains challenging in low-texture regions, where the absence of distinct features complicates reliable correspondence. Inspired by human depth perception, which leverages prior knowledge or contextual information, enabling a more accurate understanding of scenes [41], many stereo depth models have introduced semantic constraints [42]–[44] and geometric priors [28], [45] to enhance model robustness and accuracy. While these strategies can mitigate some difficulties, they are often tailored to specific

tasks and heavily dependent on large-scale, high-quality training datasets.

Recent studies have explored joint optimization paradigms that incorporate surface normal maps. Surface normals are inherently easier to estimate and perceive from visual data, providing a straightforward and effective geometric constraint for depth estimation [4]. Gui *et al.* [46] and Hu *et al.* [4] propose joint depth-normal optimization methods that distill prior knowledge from large-scale pre-trained models. Meanwhile, Gwangbin *et al.* [47] and Shao *et al.* [48] enforce consistency constraint to refine depth predictions by recurrently aligning them with surface normal maps. However, these methods often rely on domain-specific assumptions or large pre-trained models, limiting their adaptability to Mars, which underscores the need for solutions that can operate effectively in the Martian environment.

### C. Scene Depth Estimation

Scene depth estimation also targets pixel-level depth prediction, but unlike object-centric methods, it aims to recover the depth of an entire scene comprising multiple objects and large-scale structures. This requires the network to model broader spatial context and understand the global layout, which becomes especially important in environments with weak local cues. While stereo depth estimation has achieved great success in well-textured Earth-like scenes, its performance often degrades in more challenging environments like Mars, where large-scale, texture-less regions dominate [49]. Traditional depth estimation techniques rely heavily on local correspondences and high-frequency cues, which are not reliably present in Martian landscapes. Existing neural network architectures are inherently biased towards high-frequency features, which are crucial for edge detection and texture analysis in conventional images [16], [17]. This bias hinders their ability to extract meaningful information from Martian landscapes, also highlights the importance of leveraging frequency domain information to improve depth estimation. Most recent works [50], [51] have emphasized high-frequency signals to preserve edges and textures, achieving more clearer boundary preservation. However, these strategies are less effective in Mars. Mars presents unique challenges due to its predominantly texture-less terrain and smooth, low-frequency patterns. In this work, our approach concentrates on enhancing the representation of low-frequency components and exploits the use of surface normal as an additional constraint to achieve high accuracy of Martian depth estimation.

## III. METHODOLOGY OVERVIEW

In this section, we introduce the inspiration behind our study and present the main architecture of the M<sup>3</sup>Depth model.

### A. Preliminaries and Motivation

**Preliminaries.** Before introducing the architecture of our model, we first review the traditional stereo matching process, as it forms the foundation of our approach.

Traditional stereo matching aims to estimate depth by emulating the human binocular vision system [52]. As illustrated

in Fig. 2, this process typically involves four key stages: feature volume construction, cost volume computation, cost volume aggregation, and disparity refinement [53]. Generally, the objective is formulated as an optimization problem that aims to minimize pixel-wise depth discrepancies for more accurate depth estimation [41].

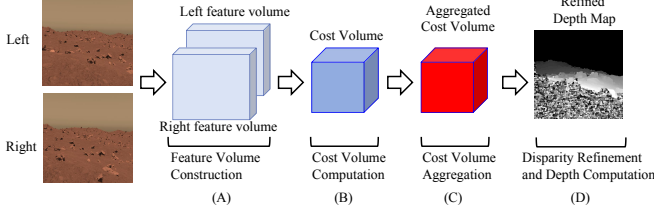


Fig. 2. Traditional stereo matching algorithm pipeline.

In the initial step, a feature extraction operator is applied to both the left and right images to generate feature descriptors for each pixel, resulting in the construction of the feature volume. After features are extracted, matching cost computation identifies correspondences by calculating the similarity between pixels in stereo image pairs, where the cost represents the similarity measure. Cost volume aggregation involves smoothing or regularizing to reduce local noise and reinforce consistent disparity patterns [54]. After the optimal disparity for each pixel is initially chosen (often determined by choosing the disparity with the minimum cost, a strategy known as *Winner-Take-All*), disparity refinement applies post-processing techniques such as median filtering to smooth the disparity map and correct small errors. Finally, disparity values are converted to depth using the known baseline  $B$  and focal length  $f$  of the stereo camera setup, given as:

$$Depth = \frac{f \times B}{Disparity}. \quad (1)$$

**Inspiration 1.** Martian surface images inherently possess sparse and subtle texture information, with highly uniform surface colors and similar features across different regions. These characteristics significantly hinder the extraction of distinct features necessary for accurate depth estimation.

To illustrate this, we first use a local binary pattern (LBP) [55] grayscale image to visualize the texture within different types of images. As shown in Fig. 3, the Mars image (left) reveals minimal texture details, characterized by a smooth, low-detail surface structure, whereas the terrestrial image (right) displays more distinct textures outline in its LBP grayscale visualization. To further analyze the frequency domain characteristics, we applied a Fourier Transform to both images. The Fourier Transform results in Fig. 3(c) and Fig. 3(d) demonstrate that the Martian image data primarily cluster within the low-frequency region, indicating that its surface features lack sharp variations or high-frequency details. In contrast, the terrestrial image exhibits a broader spectrum of frequency components, with significant high-frequency signals distributed throughout the Fourier space.

However, existing neural network architectures, particularly convolutional layers, tend to respond primarily to high-frequency signals [16], [17]. This tendency can result in

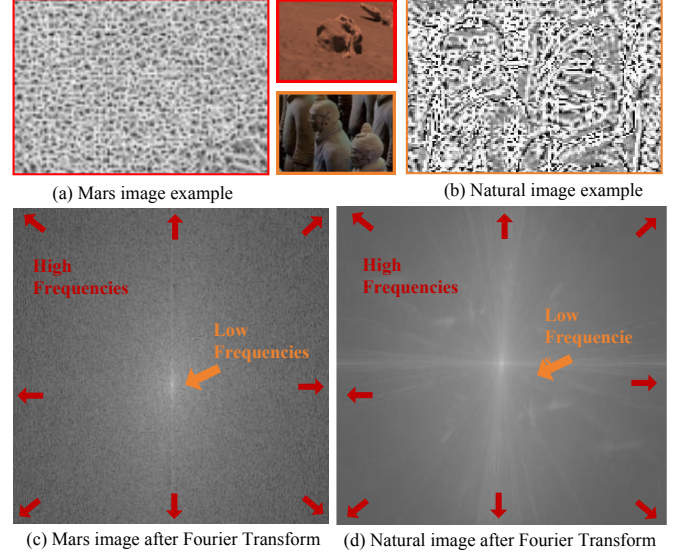


Fig. 3. A comparison between a Martian image and a terrestrial image. Subfigures (a) and (b) show the corresponding LBP grayscale versions. Subfigures (c) and (d) depict the Fourier Transform of original images.

an inherent bias that undervalues low-frequency information, which is crucial in Martian surface images.

These discussions above raise the first inspiration for the model design: *Can we leverage signal-processing techniques to effectively improve the feature extraction of low-frequency regions?*

**Inspiration 2.** In addition to the challenges posed by texture-less regions on Martian surface, we observe that surface normal maps are much easier to infer from visual appearances compared to depth maps. As illustrated in Fig. 4, learning-based methods produce significantly more detailed and accurate predictions for surface normals than for depth maps, as surface normals primarily capture local geometric properties such as orientation and smoothness. In contrast, depth estimation requires integrating global spatial relationships and scene structure, demanding a comprehensive understanding of the broader image context. This phenomenon is especially pronounced on Mars, where homogeneity and the absence of distinct edges make it challenging to infer accurate depth values.

Notably, the geometric relationship between surface normals and depth is inherently complementary. Surface normal map provides local orientation, which can guide and constrain depth estimation by providing geometric priors. A clear illustration of their interdependence is that, given an accurate depth estimate for a pixel  $i$ , the depth of its neighboring pixel  $j$  can be inferred using the surface normal map [56].

These observations above inspire the second inspiration about the model design motivation: *Can we leverage the surface normal as another modal data to boost the depth estimation in feature-sparse environments?*

## B. Model Framework Overview

In this section, we introduce the detailed end-to-end pipeline of our proposed M<sup>3</sup>Depth model, as depicted in Fig. 5. The

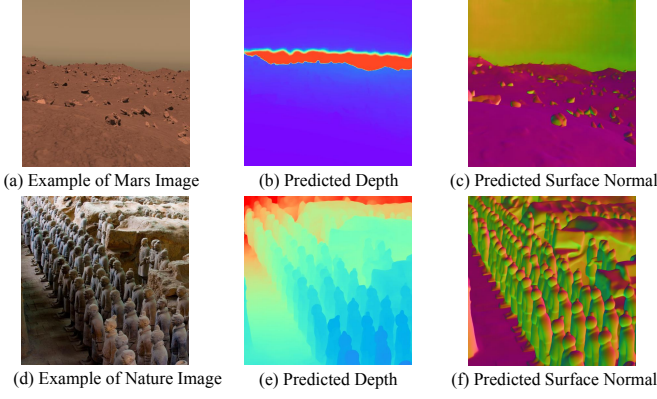


Fig. 4. A comparison of depth estimation and surface normal prediction results for Martian (top row) and terrestrial (bottom row) images. (a) and (d) are the original images; (b) and (e) show the predicted depth maps, while (c) and (f) depict the predicted surface normal maps.

network is designed to estimate depth maps from stereo image pairs. Generally, our pipeline consists of multiple key stages, including feature extraction, 4D cost volume construction and cost aggregation, surface normal prediction, and the depth refinement module that incorporates surface normals as geometric constraints.

The pipeline begins with a shared 2D CNN-based feature extraction network enhanced by wavelet transforms, applied separately to the left and right images to generate feature representation. The extracted feature maps from the left and right images are then concatenated to construct an initial 4D feature cost volume  $C_0$ , with dimensions defined as  $f \times D \times H \times W$ , where  $f$  denotes the feature dimensions,  $D$  is the disparity dimension, and  $H, W$  represent the image height and width, respectively. This cost volume encodes raw matching costs across all possible disparity levels and serves as the foundation for depth estimation. Subsequently, the initial feature cost volume  $C_0$  is refined through a series of 3D CNNs to generate feature cost volume  $C_1$ . Then,  $C_1$  is further processed with additional 3D CNN layers to produce a probability cost volume  $P_1$ , which reflects the disparity probabilities for each pixel. Further cost aggregation is performed, yielding a more precise probability cost volume  $P_2$ . Finally, the final probability cost volume  $P_2$  is used to compute an initial depth map  $D_0$  via a soft argmin operation over the disparity probabilities.

The surface normal map, used as an additional geometric constraint, is estimated through a dedicated Surface Normal Network (SSNet), as illustrated in Fig. 8. Then, the initial depth map and the surface normal map are jointly input into the iterative refinement module. To achieve iterative refinement, a ConvGRU-based refinement module is utilized to incrementally update the predicted depth map. During each iteration, each ConvGRU unit computes a residual depth map  $\Delta$ , which is then added to the previous depth estimate, updating the predicted depth map and achieving higher depth prediction accuracy.

#### IV. DETAIL MODULE DESIGN

In this section, we present three main parts of our M<sup>3</sup>Depth in detail, including the wavelet-enhanced feature extractor,

consistency constraint formulation and iterative refinement module. Additionally, we describe the supervised learning strategy in our framework, including the training objective, the design of loss functions, and the incorporation of geometric priors to effectively guide the training process.

##### A. Wavelet-Enhanced Feature Extractor

In Martian depth perception, where multiple objects are present, a larger receptive field is required [57] to effectively capture and infer contextual information compared to conventional depth perception. Conventional convolutional layers prioritize high-frequency information, such as edges and textures, but often neglect low-frequency components that are critical for smooth regions and global context [16], [17]. Inspired by this limitation, we incorporate the Wavelet Transform (WT), a signal processing method that decomposes an image into components with varying frequencies [58] into the feature extraction module to simultaneously capture multi-frequency information while expanding the receptive field.

**Wavelet-Enhanced Convolution.** We extend the 1-D Wavelet Transform to 2-D image processing by applying the transform separately along both the horizontal and vertical dimensions of the image. This approach results in a depth-wise convolution operation with a stride of 2. Specifically, we use a filter set  $\mathcal{F}_{WT} \triangleq [f_A, f_H, f_V, f_D]$ , consisting of four filters:

$$\begin{aligned} f_A &= \frac{1}{2} \begin{bmatrix} 1 & 1 \\ 1 & 1 \end{bmatrix}, f_H = \frac{1}{2} \begin{bmatrix} 1 & -1 \\ 1 & -1 \end{bmatrix}, \\ f_V &= \frac{1}{2} \begin{bmatrix} 1 & 1 \\ -1 & -1 \end{bmatrix}, f_D = \frac{1}{2} \begin{bmatrix} 1 & -1 \\ -1 & 1 \end{bmatrix}. \end{aligned} \quad (2)$$

Here,  $f_A$  captures low-frequency information, while  $f_H, f_V$ , and  $f_D$  are designed for extracting high-frequency components along the horizontal, vertical, and diagonal directions, respectively. As illustrated in Eq.(3), for each input channel, the convolution outputs four channels, each with half the resolution of the input  $X$ .

$$\text{Output} \triangleq [X_A, X_H, X_V, X_D] = \text{Conv}(\mathcal{F}_{WT}, X), \quad (3)$$

where  $X_A$  denotes the low-frequency component.  $X_H, X_V, X_D$  represent the extracted horizontal, vertical, and diagonal high-frequency components, respectively. For simplicity, we collectively represent them as  $\mathcal{F}_{HF} \triangleq [X_H, X_V, X_D]$ .

Due to the kernels in  $\mathcal{F}_{WT}$  form a set of orthonormal basis, the orthogonality property of these filters imply that the filtered signals can be inverted using the inverse wavelet transform (IWT), which is essentially the transposed convolution [59]. Hence, the IWT is equivalent to performing transposed convolution, denoted as  $\text{Conv}^T$ :

$$X = \text{Conv}^T(\mathcal{F}_{WT}, \text{Output}). \quad (4)$$

**Cascading Decomposition and Integration.** To implement the cascade of wavelet decomposition, we recursively apply the WT to decompose the low-frequency component at each level. After each level of the decomposition, the low-frequency signal is progressively decomposed as follows:



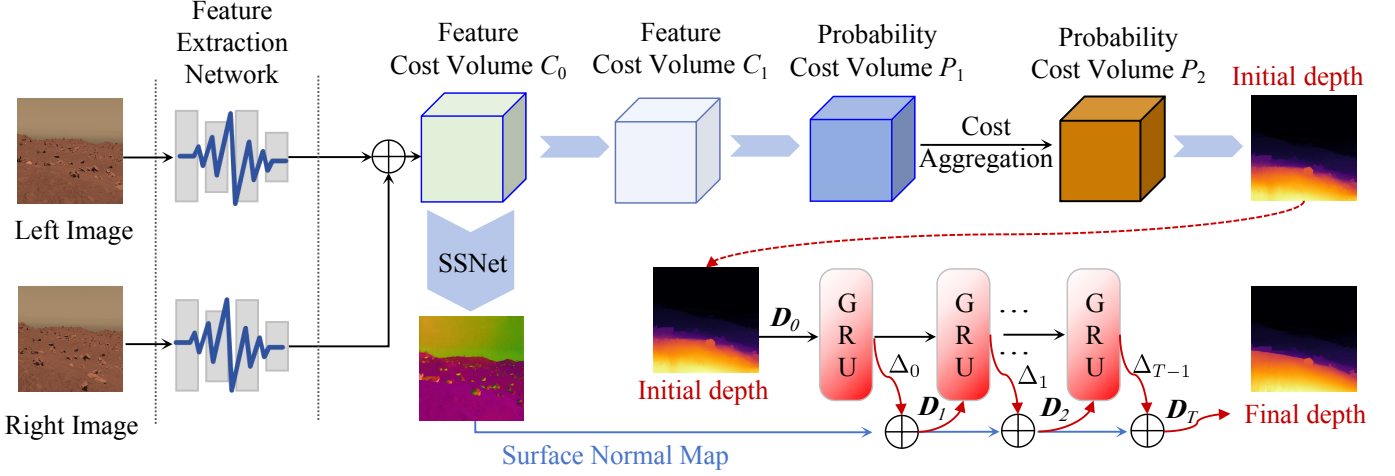


Fig. 5. Overview of our M³Depth model. In our model, the left image is served as the reference image and the right image as the target image. The cost volumes are constructed based on the wavelet-enhanced feature extraction network. Depth and surface normal are jointly optimized with a mutual-boosting manner.

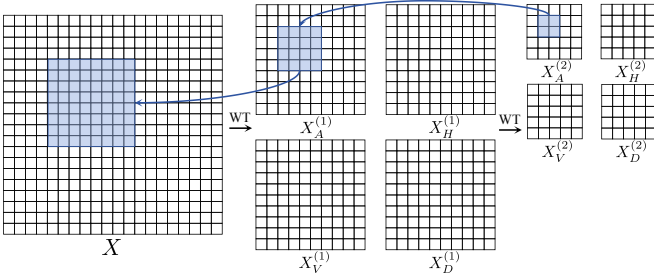


Fig. 6. Illustration of hierarchical decomposition using wavelet transform. The diagram demonstrates the process of dividing an image across multiple levels, emphasizing the progressive increase in receptive field size.

$$X_A^{(i)}, X_H^{(i)}, X_V^{(i)}, X_D^{(i)} = WT(X_A^{(i-1)}), \quad (5)$$

where  $X_A^{(i)}$  denotes the current low-frequency component, and  $i$  is the decomposition level.

To mitigate increasing the number of model parameters, the WT operation is employed to filter and downscale the input images. Specifically, the input image is first decomposed into low-frequency and high-frequency components using WT, followed by applying a depth-wise convolution with small kernels to each component. To enhance the low-frequency feature extraction, we recursively decompose and integrate the low-frequency component at each level. At each decomposition level, all frequency components are processed following the cascading principle in Eq.(5). Therefore, the wavelet-enhanced convolution operation can be formulated as follows:

$$Y_A^{(i)}, Y_{HF}^{(i)} = Conv(W^{(i)}, (X_A^{(i)}, \mathcal{F}_{HF}^{(i)})). \quad (6)$$

Here  $W^{(i)}$  denotes the weight tensor for a  $k \times k$  convolution kernel, while  $X_A^{(i)}$  corresponds to the low-frequency component at level  $i$ .  $\mathcal{F}_{HF}^{(i)}$  represents the other three high-frequency component of level  $i$  (i.e.  $X_H^{(i)}, X_V^{(i)}, X_D^{(i)}$ ).

To merge the outputs of the different frequency components, we exploit the linearity properties of the WT and IWT, i.e.

$IWT(X + Y) = IWT(X) + IWT(Y)$ . The core objective of preserving more low-frequency information is to amplify these low-frequency components by combining the current level low-frequency components with the previous level low-frequency output. The repeated WT decomposition of the low-frequency components emphasizes them and increases the corresponding response towards low-frequency components. Specifically, this process is explicitly formulated as follows:

$$Z^{(i)} = IWT(Y_A^{(i)} + Z^{(i+1)}, Y_{HF}^{(i)}), \quad (7)$$

where  $Y_A^{(i)}$  is the low-frequency component at level  $i$ ,  $Y_{HF}^{(i)}$  represents the high-frequency components at level  $i$ , and  $Z_i$  is the aggregated outputs from level  $i$  onward. This process ensures that more low-frequency components are preserved across the levels of decomposition. The overall operation details are illustrated in Algorithm 1.

**Receptive Fields Analysis.** To demonstrate the effect of our wavelet-based approach on receptive field expansion, we analyze how the wavelet decomposition influences the receptive field of convolutional operations. In traditional convolutional operations, the receptive field size increases linearly with kernel size and depth. However, wavelet decomposition inherently down-samples the spatial dimensions while preserving essential structural information. This results in a significant increase in the effective receptive field when convolution is performed in the wavelet domain. For example, in Fig. 6 performing a  $2 \times 2$  convolution on the second-level low-frequency component  $X_A^{(2)}$  corresponds to an effective receptive field of  $8 \times 8$  in the original input space. Each successive wavelet decomposition level doubles the receptive field size, allowing our model to capture global contextual information more efficiently. Theoretically, the receptive field size is expanding exponentially as the decomposition level  $i$ , that is  $(2^i \cdot k)$ , where  $k$  denotes the kernel size. By reducing the resolution through decomposition, the model can process larger receptive fields with fewer parameters and reduced computational cost, achieving a balance between efficiency and accuracy.

---

**Algorithm 1** Wavelet-Enhanced Convolution with Cascading Decomposition and Integration.

---

**Input:**  $X \in \mathbb{R}^{C \times W \times H}$ .

**Output:**  $Z^{(0)} \in \mathbb{R}^{C \times W \times H}$ .

```

1:  $X_A^{(0)} = X$ 
2:  $Y_A^{(0)} = \text{Conv}(W^{(0)}, X_A^{(0)})$ 
3: for  $i = 1, \dots, \ell$  do
4:    $X_A^{(i)}, X_H^{(i)}, X_V^{(i)}, X_D^{(i)} = WT(X_A^{(i-1)})$ 
5:    $Y_A^{(i)}, Y_H^{(i)}, Y_V^{(i)}, Y_D^{(i)} =$ 
      $\text{Conv}(W^{(i)}, (X_A^{(i)}, X_H^{(i)}, X_V^{(i)}, X_D^{(i)}))$ 
6: end for
7:  $Z^{(\ell+1)} = 0$ 
8: for  $i = \ell, \dots, 1$  do
9:    $Z^{(i)} = IWT(Y_A^{(i)} + Z^{(i+1)}, Y_H^{(i)}, Y_V^{(i)}, Y_D^{(i)})$ 
10: end for
11:  $Z^{(0)} = Y_A^{(0)} + Z^{(1)}$ 

```

---

### B. Consistency Constraint Formulation

To jointly optimize the depth and surface normal predictions within our model framework, we introduce a consistency constraint to enforce the geometric alignment between the two maps. Leveraging the pinhole camera model, we establish the geometric correlation between depth and surface normal and then derive the consistency constraint from their intrinsic geometric correlation.

Under the pinhole camera model, the spatial gradient of the depth map in the pixel coordinate system is computed by integrating information from both the depth and surface normal maps. As illustrated in Fig. 7,  $(u, v)$  represents the pixel coordinate corresponding to the 3D point  $(X, Y, Z)$ , and  $(u_c, v_c)$  denotes the pixel coordinate of the camera's optical center. Additionally,  $f_x$  and  $f_y$  represent the focal lengths along the X-axis and Y-axis, respectively.

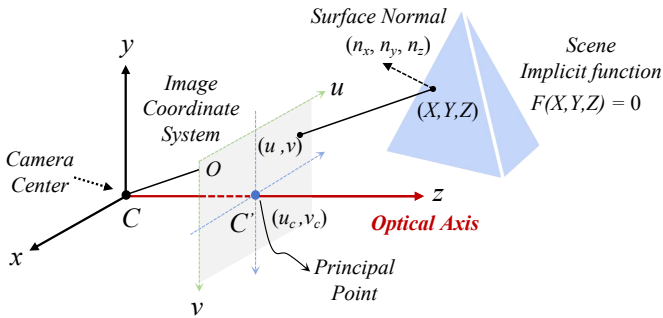


Fig. 7. Pinhole camera model and the scene implicit function.

Based on fundamental principles of photogrammetry, the pixel coordinates  $(u, v)$  can be transformed into three-dimensional spatial coordinates  $(X, Y, Z)$ , as Eq.(8) depicts.

$$\begin{bmatrix} u \\ v \\ 1 \end{bmatrix} = \frac{1}{Z} \begin{bmatrix} f_x & 0 & u_c \\ 0 & f_y & v_c \\ 0 & 0 & 1 \end{bmatrix} \begin{bmatrix} X \\ Y \\ Z \end{bmatrix}. \quad (8)$$

Based on the pinhole camera model and the chain rule, we can yield equation below:

$$\begin{cases} \frac{\partial X}{\partial v} = \frac{u - u_c}{f_x} \frac{\partial Z}{\partial v} \\ \frac{\partial Y}{\partial v} = \frac{v - v_c}{f_y} \frac{\partial Z}{\partial v} + \frac{Z}{f_y} \end{cases} \quad (9)$$

Depth and surface normal information are inherently related through the geometry of the 3D scene. To ensure consistency between these two modalities, we consider two types of constraints as follows. Due to space limitations, the detailed derivation of the geometric relationship and constraint formulation is provided in the [Appendix](#).

#### Constraints 1: Geometric Mathematical Constraint.

The first constraint is derived from the mathematical relationship between depth gradients and surface normals. The surface normal can be expressed as the gradient of an implicit function, and this relationship provides a direct linkage between depth gradients and normal vectors.

Under the surface function assumption, the scene can be represented as an implicit function  $F(X, Y, Z) = 0$ . The surface normal map, denoted as  $\vec{n} = (n_x, n_y, n_z)$ , can be interpreted as the gradient of this function:

$$\nabla F = \left( \frac{\partial F}{\partial X}, \frac{\partial F}{\partial Y}, \frac{\partial F}{\partial Z} \right) = (n_x, n_y, n_z). \quad (10)$$

Then, we can yield equation below:

$$\left( \frac{\partial Z}{\partial u} \right)_1 = \frac{\left( \frac{-n_x Z}{n_z f_x} \right)}{1 + \frac{n_x}{n_z} \frac{u - u_c}{f_x} + \frac{n_y}{n_z} \frac{v - v_c}{f_y}}. \quad (11)$$

$$\left( \frac{\partial Z}{\partial v} \right)_1 = \frac{\left( \frac{-n_y Z}{n_z f_y} \right)}{1 + \frac{n_x}{n_z} \frac{u - u_c}{f_x} + \frac{n_y}{n_z} \frac{v - v_c}{f_y}}. \quad (12)$$

#### Constraint 2: Spatial Gradient Constraint.

The spatial gradient of the depth map can be efficiently estimated using standard image processing techniques, such as the Sobel filter, which approximates local depth variations in the image. This gradient captures changes in depth along the horizontal and vertical directions, providing a data-driven estimate of the surface geometry structure. The spatial gradient of the depth map can be computed by using a Sobel filter:

$$\left( \frac{\partial Z}{\partial u}, \frac{\partial Z}{\partial v} \right)_2 = \left( \frac{\Delta Z}{\Delta u}, \frac{\Delta Z}{\Delta v} \right). \quad (13)$$

The consistency constraint is formulated as deviation between the two constraints of  $\left( \frac{\partial Z}{\partial u}, \frac{\partial Z}{\partial v} \right)_1$  and  $\left( \frac{\partial Z}{\partial u}, \frac{\partial Z}{\partial v} \right)_2$ . The consistency constraint is further formulated as a consistency loss function, enabling it to guide model training by aligning the two gradient estimates. This loss is defined as the Huber norm of their deviation, as shown in Eq.(14).

$$\mathcal{L}_c = \left| \left( \frac{\partial Z}{\partial u}, \frac{\partial Z}{\partial v} \right)_1 - \left( \frac{\partial Z}{\partial u}, \frac{\partial Z}{\partial v} \right)_2 \right|_{\mathbf{H}}. \quad (14)$$

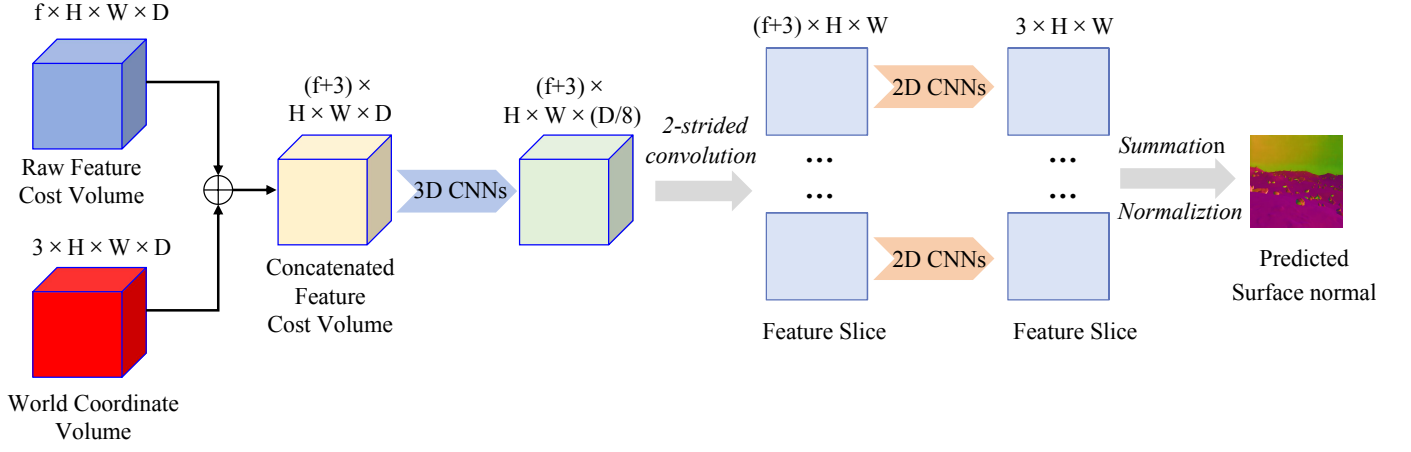


Fig. 8. Overview of the surface normal prediction network. The outputs are summed and normalized to generate the final predicted surface normal map.

### C. Surface Normal Map Prediction

Surface normal provides important geometric information for 3D scene perception. Unlike stereo depth estimation, surface normal maps are not influenced by scale ambiguity and operate within a compact output space (a unit sphere vs. positive real value for depth). Furthermore, surface normal estimation methods show strong generalization when applied in out-of-distribution images [60], which makes our approach both feasible and effective.

To address the inherent ambiguity in depth estimation, the depth range is discretized into multiple depth slices, each corresponding to a specific depth hypothesis. Since the surface normal at a pixel is determined by the orientation of the surface at its true depth, the accuracy of normal prediction relies on the alignment between depth hypotheses and the true depth of the surface. Slices closer to the true depth contribute more accurate local geometric information, while slices farther away contribute less and are effectively suppressed.

In our model, we employ the slice-based surface normal prediction network, denoted as  $SSNet(S_i)$ , which utilizes the feature cost volume  $C_0$  to predict the surface normal map. As shown in Fig. 8, the cost volume encapsulates both spatial and visual feature information, forming the foundation for surface normal estimation. The concatenated feature volume  $(f+3) \times H \times W \times D$  is processed by three layers of 3D convolutions with a stride of 2 along the depth dimension, reducing its size and generating a compact representation while preserving key spatial features. Following this, the processed feature volume is sliced along the depth dimension into  $\frac{D}{8}$  feature slices. Each slice-specific 2D CNN predicts a preliminary surface normal map for its corresponding depth hypothesis. The final normal map,  $\vec{n}$ , is computed by summing the normal estimates from all slices and normalizing the result, as shown by:

$$\vec{n} = \frac{\sum_{i=1}^{D/8} SSNet(S_i)}{\left\| \sum_{i=1}^{D/8} SSNet(S_i) \right\|_2}. \quad (15)$$

### D. Iterative Refinement Module

To facilitate the mutual boosting across depth and surface normal predictions, we implement a learning-based optimization with recurrent refinement blocks, as illustrated in Fig. 5. Unlike previous methods [28], our approach iteratively updates both depth and surface normals through a unified refinement process.  $\hat{D}^t$  and  $\hat{N}^t$  represent the depth map and surface normal map refined at iteration step  $t$ , where  $t \in [0, 1, \dots, T]$  denotes the iteration index. Inspired by [4], [61], we adopt a convolutional gated recurrent unit (ConvGRU) to yield these updates, since the ConvGRU can memorize the history states and make full use of the temporal information during the refinement process.

Grounded on the initial predictions,  $\hat{D}^0$  and  $\hat{N}^0$ , the depth and surface normal maps are iteratively refined using updates  $\Delta\hat{D}^{t+1}$  and  $\Delta\hat{N}^{t+1}$  at each step. In general, the refinement process is governed by a recurrent block  $\Phi$ , which computes updates for both depth and surface normal predictions, as follows:

$$\Delta\hat{D}^{t+1}, \Delta\hat{N}^{t+1}, \mathbf{H}^{t+1} = \Phi(\hat{D}^t, \hat{N}^t, \mathbf{H}^t, \mathbf{H}^0), \quad (16)$$

where  $\mathbf{H}^t$  denotes the hidden feature state at iteration  $t$ . The depth and surface normals are updated iteratively as:

$$\hat{D}^{t+1} \leftarrow \hat{D}^t + \Delta\hat{D}^t, \hat{N}^{t+1} \leftarrow \hat{N}^t + \Delta\hat{N}^t, \quad (17)$$

where  $\Delta\hat{D}^t$  and  $\Delta\hat{N}^t$  represent the respective updates at iteration  $t$ .

In our model design, the recurrent block  $\Phi$  consists of a ConvGRU sub-block and two projection heads,  $\Phi_d$  and  $\Phi_n$ , which predict updates  $\Delta\hat{D}^{t+1}$  and  $\Delta\hat{N}^{t+1}$  respectively. Specifically:

$$\begin{cases} \Delta\hat{D}^{t+1} = \Phi_d(\hat{D}^t, \mathbf{H}^t, \mathbf{H}^0), \\ \Delta\hat{N}^{t+1} = \Phi_n(\hat{D}^t, \mathbf{H}^t, \mathbf{H}^0), \end{cases} \quad (18)$$

where  $\mathbf{H}^{t+1}$  is the updated hidden state computed by the ConvGRU, combining the information from the current depth and surface normal maps:



$$\mathbf{H}^{t+1} = \text{ConvGRU}(\hat{\mathbf{D}}^t, \hat{\mathbf{N}}^t, \mathbf{H}^0, \mathbf{H}^t). \quad (19)$$

After  $T$  refinement steps, the process yields the final optimized depth map  $\hat{\mathbf{D}}^T$  and surface normal map  $\hat{\mathbf{N}}^T$ , capturing the synergistic relationship between the two modalities for improved accuracy.

### E. Supervision Formulation

To improve the accuracy and smoothness of the depth estimation, we integrate multiple complementary loss functions into the training process. These losses are designed to leverage both pixel-wise supervision and geometric consistency between depth and surface normals. Altogether, our approach incorporates the following three key loss functions during model training:

- 1) *Pixel-Wise Depth Loss*  $\mathcal{L}_d$ : measures the discrepancy between the predicted depth map  $\hat{\mathbf{D}}$  and the ground truth depth map  $\mathbf{D}_{gt}$ , aiming to minimize the pixel-wise depth error.
- 2) *Pixel-Wise Surface Normal Loss*  $\mathcal{L}_n$ : quantifies the difference between the predicted surface normal map  $\hat{\mathbf{N}}$  and the ground truth normals  $\mathbf{N}_{gt}$ , ensuring accurate prediction of surface normal.
- 3) *Consistency Constraint Loss*  $\mathcal{L}_c$ : enforces geometric consistency between the depth map and surface normal predictions, as Eq.(14) shows.

The depth loss  $\mathcal{L}_d$  and surface normal loss  $\mathcal{L}_n$  are both defined using the Huber norm, which provides robust handling of outliers by balancing between the squared error for small deviations and the absolute error for larger deviations. Taking depth as an example, the per-pixel error  $e(i, j)$  is computed as:

$$e(i, j) = \hat{\mathbf{D}}(i, j) - \mathbf{D}_{gt}(i, j), \quad (20)$$

where  $\hat{\mathbf{D}}(i, j)$  represents the predicted depth at pixel  $(i, j)$ , and  $\mathbf{D}_{gt}(i, j)$  denotes the corresponding ground truth depth value. The Huber loss is then applied to this error:

$$\mathcal{L}_\delta(e(i, j)) = \begin{cases} \frac{1}{2}e(i, j)^2 & \text{if } |e(i, j)| \leq \delta, \\ \delta \cdot (|e(i, j)| - \frac{1}{2}\delta) & \text{if } |e(i, j)| > \delta. \end{cases} \quad (21)$$

For depth, the total loss is computed as the average over all pixels:

$$\mathcal{L}_d = \frac{1}{N} \sum_{i,j} \mathcal{L}_\delta(e(i, j)), \quad (22)$$

where  $N$  is the total number of pixels.

The final loss function incorporates all three components:

$$\mathcal{L}_{overall} = \lambda_d \mathcal{L}_d + \lambda_n \mathcal{L}_n + \lambda_c \mathcal{L}_c, \quad (23)$$

where  $\lambda_d$ ,  $\lambda_n$ , and  $\lambda_c$  are weights balancing the contributions of the depth loss, normal loss, and consistency loss.

Our M<sup>3</sup>Depth model involves training a unified predictor  $\mathcal{N}_{d-n}$  to predict depth map  $\hat{\mathbf{D}}$  and surface normal map  $\hat{\mathbf{N}}$  from a given set of images  $\mathbf{I} = \{(\mathbf{I}_L^i, \mathbf{I}_R^i), i \in [1, 2, \dots, M]\}$ ,

where  $\mathbf{I}_L^i$  and  $\mathbf{I}_R^i$  represent the left and right images of the  $i$ -th stereo pair, respectively, and  $M$  denotes the total number of stereo pairs in the dataset.

The primary objective is to ensure that the predicted depth map  $\hat{\mathbf{D}}$  aligns closely with the true depth map  $\mathbf{D}_{gt}$ . Formally, the end-to-end prediction process can be formulated as:

$$\hat{\mathbf{D}}, \hat{\mathbf{N}} = \mathcal{N}_{d-n}(\mathbf{I}, \theta), \quad (24)$$

where  $\theta$  represents the network parameters. The training objective is to identify the optimal parameters  $\theta^*$  which minimize the overall loss function  $\mathcal{L}_{overall}$ , defined as:

$$\theta^* = \arg \min_{\theta} \{\mathcal{L}_{overall}(\mathcal{N}_{d-n}(\mathbf{I}, \theta), \mathbf{D}_{gt}, \mathbf{N}_{gt})\}. \quad (25)$$

## V. EXPERIMENTS

We perform comprehensive experiments using Mars datasets, including both a synthetic Mars dataset and real-world scenario captured by Zhurong Rover. In this section, we first give an overview of the datasets, comparison models, evaluation metrics, and experiment training details. Next, we present both quantitative and qualitative comparisons with current state-of-the-art (SOTA) competitors. To validate the efficacy of each key component, we conduct ablation studies both quantitative and qualitative. Finally, we discuss potential applications and highlight the future works.

### A. Experimental Implementation

1) *Datasets*: Our study leverages the SimMars6K dataset [10] to train and evaluate our proposed model, which comprises 6325 pairs of simulated stereo images with depth labels, generated using the OAISYS simulator. This dataset is designed to closely replicate Martian terrain and aligns with the configurations of the Navigation and Terrain Camera (NaTeCam) on China's Zhurong Rover.

The stereo camera setup mirrors the real-world specifications of NaTeCam used on Zhurong Rover. It is mounted 1.2 meters above the ground surface, with a baseline of 270 mm, a focal length of 595.90 pixels, and a field of view (FoV) measuring  $46.5^\circ \times 46.5^\circ$ . The captured images are all with a resolution of  $512 \times 512$  pixels, ensuring consistency with the rover's real-world imaging capabilities.

Following the guidelines in [32], the camera can capture a depth field ranging from 0.5 meters to infinity, with optimal focus at 1 meters. To ensure the practicality in real-world scenarios, only areas within a 15 meters capture radius are considered in this study, excluding regions beyond this range or at infinite depth [62]. As shown in Fig. 9, each stereo image pair consists of left and right perspective images. The left image is used as the reference image, and its depth ground truth is processed accordingly. The cumulative distribution function of the depth values is illustrated in Fig. 9.(d), revealing that approximately 90% of the pixel values are within a range of 15 meters. Additionally, we follow these established methods described in [4], [28], [63] to generate ground truth surface normal for training<sup>1</sup>.

<sup>1</sup>The processed dataset, including depth and surface normal labels, is publicly available at <https://zenodo.org/records/14286916>.

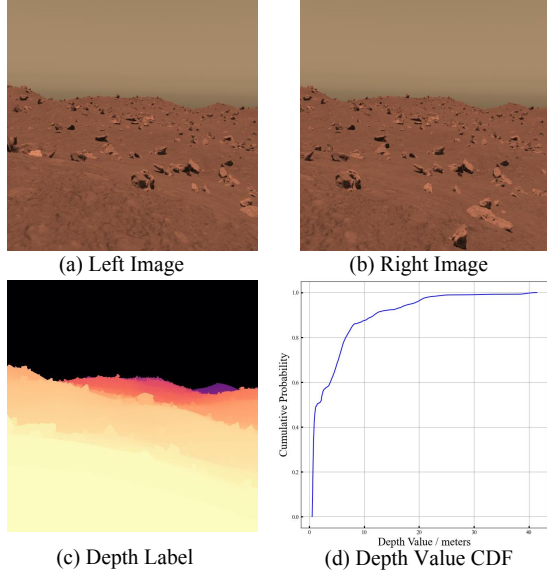


Fig. 9. Visualization of dataset examples and depth distribution characteristics.

2) *Comparison Models*: To verify the advantages of our proposed depth estimation model, we use following SOTA methods for comparison:

- Raft-Stereo [61]: employs multi-level convolutional GRUs to iteratively propagate and aggregate contextual information across the image, facilitating precise stereo correspondence estimation.
- HitNet-Stereo [64]: replaces traditional cost volume construction with a multi-resolution initialization strategy. It employs differentiable 2D geometric propagation and warping mechanisms, while leveraging slanted plane hypotheses for accurate disparity estimation.
- CRE-Stereo [65]: employs a hierarchical coarse-to-fine disparity refinement with a cascaded recurrent architecture and an adaptive group correlation layer to address rectification errors, enabling robust stereo matching.
- UniMVSNet-Stereo [66]: introduces a unified depth representation combining regression and classification advantages, along with a Unified Focal Loss to address sample imbalance, enabling fine-grained, sub-pixel depth estimation without additional computational overhead.
- Selective-Stereo [50]: utilizes selective recurrent unit, an iterative update operator that adaptively fuses multi-frequency disparity information for edges and smooth regions using a contextual spatial attention module.

3) *Evaluation Metrics*: To quantitatively evaluate the performance of the proposed framework and comparative approaches from various aspects, our study evaluates the models using widely adopted metrics in depth estimation. The commonly used evaluation metrics are defined as follows:

- Absolute Relative Error (Abs Rel): computes the mean of relative errors between the predicted depth and the

ground truth depth:

$$\text{Abs Rel} = \frac{1}{N} \sum_j \frac{|\hat{d}_j - d_j|}{d_j}. \quad (26)$$

- Squared Relative Error (Sq Rel): defined as the average squared error ( $L_2$  distance) between the ground-truth depth and the predicted depth, normalized by the ground-truth depth value for each pixel:

$$\text{Sq Rel} = \frac{1}{N} \sum_j \frac{|\hat{d}_j - d_j|^2}{d_j}. \quad (27)$$

- Root Mean Squared Error (RMSE): measures the square root of the mean squared differences between predicted and ground truth depths:

$$\text{RMSE} = \sqrt{\frac{1}{N} \sum_j |\hat{d}_j - d_j|^2}, \quad (28)$$

- $\log_{10}$ : computes the mean of the logarithmic differences between the predicted depth and the ground truth depth:

$$\log_{10} = \frac{1}{N} \sum_{j=1}^N \left| \log_{10} \hat{d}_j - \log_{10} d_j \right|. \quad (29)$$

- Threshold Accuracy ( $\delta_i$ ): calculates the percentage of pixels that satisfy the following condition:

$$\max \left( \frac{d_j}{\hat{d}_j}, \frac{\hat{d}_j}{d_j} \right) = \delta < \delta_i = 1.25^i, i \in [1, 2, 3]. \quad (30)$$

Among these,  $\hat{d}_j$  is the predicted depth of pixel  $j$ ,  $d_j$  is the ground truth of pixel  $j$  in depth label map, and  $N$  is the total number of pixels.

4) *Training Settings*: All our models are implemented using the PyTorch framework and trained on Ubuntu 18.04 system equipped with 4 NVIDIA RTX 4090 GPUs. The dataset is split into training, validation, and testing subsets with a ratio of 7:2:1. The training epochs is uniformly set to 100. The batch size is set to 12, constrained by GPU memory. During training, the model with the lowest loss on the training set is automatically saved. The Adam optimizer is used with an initial learning rate of  $1 \times 10^{-4}$  by default. In our network, the trainable parameters are initialized with a normal distribution. The ground-truth depth values of all the depth images are normalized to the range  $[0, 1]$ , which is a common preprocessing step in depth estimation tasks. The hyper-parameters, loss function weights  $\lambda_d$ ,  $\lambda_n$  and  $\lambda_c$  are set to 2, 1 and 3 respectively.

## B. Experimental Results

1) *Quantitative Results*: To compare on the SimMars6K datasets, we choose several state-of-the-art (SOTA) approaches of a diverse kind. These include iterative optimization-based methods like Raft-Stereo [61], hierarchical and geometric propagation approaches such as HitNet-Stereo [64], coarse-to-fine refinement strategies exemplified by CRE-Stereo [65],

TABLE I

QUANTITATIVE RESULTS COMPARISON ON DEPTH ESTIMATION AMONG SOTA ALGORITHMS. ALL RESULTS ARE EVALUATED ON SIMMARS6K DATASET. THE BEST RESULTS ARE MARKED IN **BOLD**.

Method	Depth Prediction Error				Depth Prediction Accuracy		
	Abs Rel ↓	Sq Rel ↓	RMSE ↓	log <sub>10</sub> ↓	$\delta_1 < 1.25 \uparrow$	$\delta_2 < 1.25^2 \uparrow$	$\delta_3 < 1.25^3 \uparrow$
Raft-Stereo [61]	0.136	0.103	0.581	0.061	0.814	0.953	0.988
HitNet-Stereo [64]	0.128	0.085	0.562	0.057	0.839	0.966	0.992
CRE-Stereo [65]	0.103	0.063	0.367	0.047	0.887	0.976	0.996
UniMVSNet-Stereo [66]	0.148	0.126	0.653	0.063	0.783	0.948	0.981
Selective-Stereo [50]	0.116	0.074	0.416	0.051	0.856	0.973	0.994
<b>M<sup>3</sup>Depth (Ours)</b>	<b>0.089</b>	<b>0.058</b>	<b>0.314</b>	<b>0.038</b>	<b>0.905</b>	<b>0.991</b>	<b>0.998</b>

unified depth representation models like UniMVSNet-Stereo [66], and frequency domain-based designs such as Selective-Stereo [50]. The complete comparison on all the metrics is presented in Table I, where Metric with  $\uparrow$  indicates that higher value is preferred, and  $\downarrow$  denotes the opposite.

As summarized in Table I, our proposed method achieves the best performance across all evaluated metrics, demonstrating its effectiveness in handling the unique challenges of Mars terrains. Specifically, our method achieves Abs Rel of 0.089 and RMSE of 0.314, representing significant improvements of 13.6% and 14.5%, respectively, compared to the next-best method (CRE-Stereo). Additionally, under  $\delta_i$  thresholds, our model achieves the highest accuracy across all levels.

In comparison, UniMVSNet-Stereo demonstrates lower performance due to its reliance on a unified depth representation that combines regression and classification. It is effective for general tasks, yet struggles with fine-grained depth estimation in complex Mars terrains. Similarly, Raft-Stereo and HitNet-Stereo achieve moderate performance due to their iterative refinement and geometric propagation strategies. However, their reliance on traditional matching mechanisms limits their adaptability in texture-less regions, leading to suboptimal results. Selective-Stereo and CRE-Stereo exhibit better performance, with CRE-Stereo particularly excelling due to its hierarchical coarse-to-fine refinement and adaptive group correlation layer, which effectively addresses rectification errors and improves matching robustness. Selective-Stereo leverages frequency domain analysis and places emphasis on high-frequency signals, allowing it to represent texture-rich edges and detailed boundaries with greater clarity. However, these methods still fall short in highly challenging regions where fine-grained precision is required.

Surface normal plays a critical role in our framework, serving as an auxiliary geometric constraint to enhance depth estimation accuracy. By leveraging the intrinsic relationship between surface normals and depth gradients, our method incorporates normal predictions to refine depth estimation. Given the importance of surface normals in our approach, it is essential to ensure the accuracy and reliability of the predicted normal maps, as errors in normal predictions could directly affect the depth estimation process. To evaluate the quality of surface normal predictions, we adopt a set of standard metrics commonly used in surface normal estimation tasks, as summarized in Table II. In this context,  $N$  represents the total number of evaluated pixels, and  $\theta_i$  is the angular error between the predicted normal vector and the ground-truth normal vector at pixel  $i$ . This angular error is computed as:

$$\theta_i = \arccos\left(\frac{\hat{\mathbf{n}}_i \cdot \mathbf{n}_i}{\|\hat{\mathbf{n}}_i\| \|\mathbf{n}_i\|}\right), \quad (31)$$

where  $\hat{\mathbf{n}}_i$  is the predicted normal vector, and  $\mathbf{n}_i$  is the ground-truth normal vector. The indicator function  $\mathbf{1}(\cdot)$  outputs 1 if the condition is true and 0 otherwise.

Table III presents the quantitative evaluation of surface normal prediction across multiple methods. Notably, Fusion [67] achieves the best results across most metrics due to its reliance on origin depth information. While our approach is not specifically tailored for surface normal estimation, it still achieves competitive performance, with a mean angular error of  $20.6^\circ$  and a median angular error of  $12.3^\circ$ . These results confirm that the predicted surface normals are sufficiently accurate to serve as a reliable auxiliary modality for improving depth estimation. The performance also demonstrates the robustness of our framework in extracting geometric features without requiring explicit ground truth depth or specific optimization for surface normal estimation.

TABLE II

METRICS FOR SURFACE NORMAL EVALUATION WITH FORMULATIONS.

Metric	Formulation
Mean	$\frac{1}{N} \sum_{i=1}^N \theta_i$ , where $\theta_i$ is the angular error.
Median	$Median(\theta_1, \theta_2, \dots, \theta_N)$ .
RMSE <sub>n</sub>	$\sqrt{\frac{1}{N} \sum_{i=1}^N \theta_i^2}$ .
$11.25^\circ$	$\frac{1}{N} \sum_{i=1}^N \mathbf{1}(\theta_i < 11.25^\circ)$ .
$22.5^\circ$	$\frac{1}{N} \sum_{i=1}^N \mathbf{1}(\theta_i < 22.5^\circ)$ .
$30^\circ$	$\frac{1}{N} \sum_{i=1}^N \mathbf{1}(\theta_i < 30^\circ)$ .

TABLE III

QUANTITATIVE EVALUATION OF SURFACE NORMAL PREDICTION RESULTS.

Method	Normal Error			Normal Accuracy		
	Mean ↓	Median ↓	RMSE <sub>n</sub> ↓	$11.25^\circ \uparrow$	$22.5^\circ \uparrow$	$30^\circ \uparrow$
Fusion [67]	15.7	10.59	30.4	0.513	0.672	0.798
GeoNet [56]	23.1	15.8	38.9	0.414	0.611	0.736
<b>M<sup>3</sup>Depth</b>	<b>20.6</b>	<b>12.3</b>	<b>34.2</b>	<b>0.445</b>	<b>0.638</b>	<b>0.759</b>

2) *Qualitative Results*: In addition to the quantitative comparison, we also perform qualitative depth comparisons to



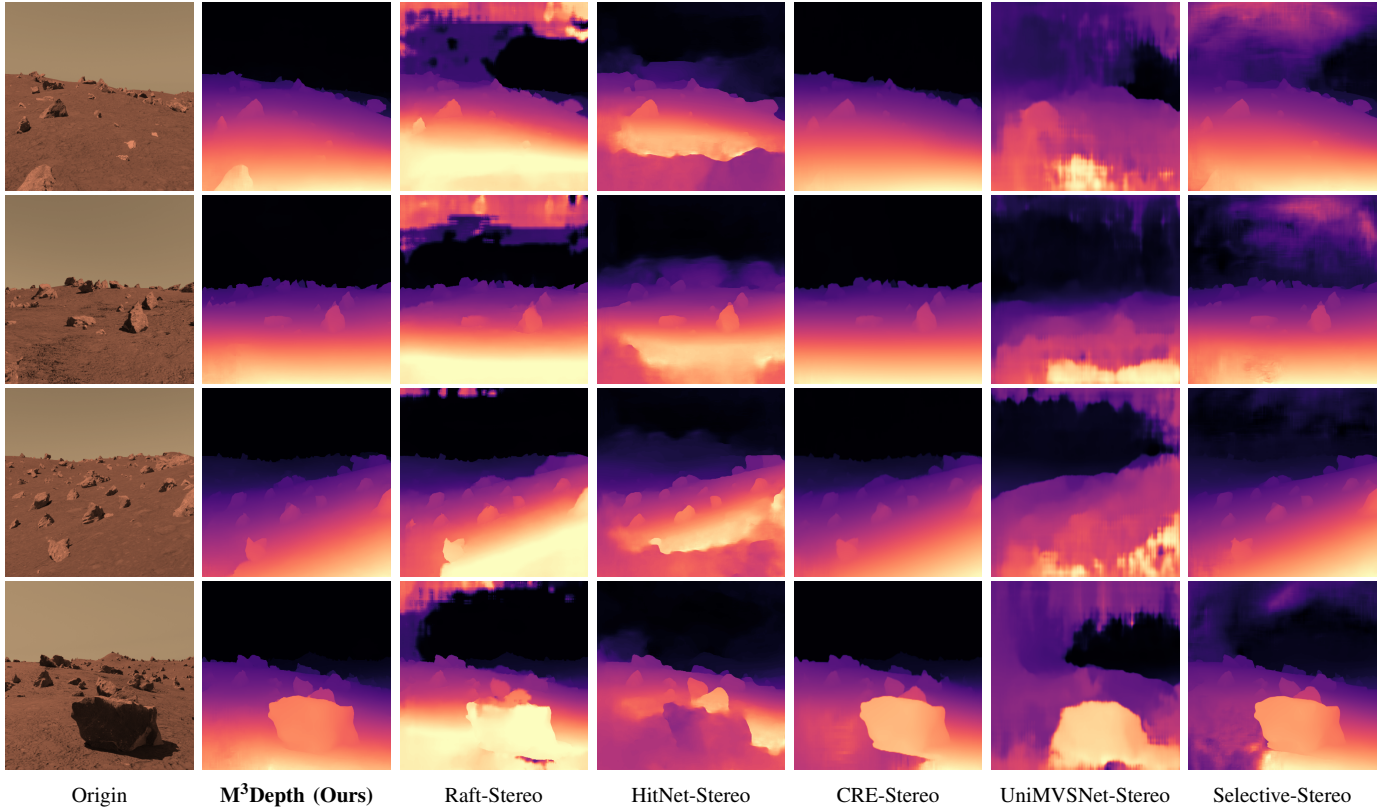


Fig. 10. Qualitative comparison of depth estimation results on Martian images. The first column shows the original reference images (left image), while the remaining columns compare the depth estimation outputs of our proposed  $M^3$ Depth model with other competitive baselines.

further validate the effectiveness of our proposed method. The qualitative analysis is conducted using the SimMars dataset, which provides a controlled environment for visualizing depth estimation performance under Martian-like conditions. Moreover, to assess the generalization ability of different methods in real-world scenarios, we extend the evaluation to real Mars imagery captured by Zhurong Rover.

As illustrated in Fig. 10, our proposed  $M^3$ Depth method demonstrates superior performance compared to state-of-the-art approaches across a variety of challenging Martian scenes. Specifically, our method excels in delineating planar regions while preserving fine-grained local details, such as edges and boundaries around rocks and terrain structures. Compared to baseline methods such as Raft-Stereo and UniMVSNet-Stereo, which exhibit artifacts and noise in texture-less regions, our  $M^3$ Depth effectively eliminates inconsistencies induced by texture-less regions and maintains geometric continuity. It is more evident in large texture-less areas and thin structures (e.g., rock edges and smooth terrain surfaces), where competing methods tend to either over-smooth the depth or introduce estimation errors.

In addition, methods like HitNet-Stereo and Selective-Stereo display a degree of improvement in handling texture variations but still struggle with depth discontinuities, especially near object boundaries. On the other hand, our method achieves sharper and more accurate transitions, demonstrating its ability to balance global structure and local details. CRE-Stereo, while performing better for coarse-level depth reconstruction,

struggles to capture fine details in areas with complex geometry or intricate surface patterns, leading to suboptimal performance in high-detail regions.

To further emphasize the strengths of our proposed  $M^3$ Depth method, we present a case study using an example from the SimMars6K dataset. As illustrated in Fig. 11, specific regions of interest are highlighted with red boxes to focus on critical depth estimation challenges, including texture-less regions, edge preservation, and anti-artifact.

- *Texture-less Regions.* In the flat terrain regions, methods like Raft-Stereo and UniMVS-Stereo exhibit noticeable noise and inconsistencies, with uneven or incorrect depth estimations. In contrast,  $M^3$ Depth produces smooth and coherent depth predictions, effectively handling the lack of texture by leveraging its wavelet-transformed convolutional kernels to capture low-frequency features.
- *Edge Preservation.* In the regions with fine geometric details and boundaries, Raft-Stereo, HitNet-Stereo, and Selective-Stereo suffer from depth bleeding and blurring, failing to delineate object boundaries accurately. CRE-Stereo, while appearing to achieve better results in such regions, struggles with sharp object edges and fine transitions. It often exhibits slight over-smoothing or loss of precision, particularly where the terrain meets the horizon or along complex geometric structures.  $M^3$ Depth, on the other hand, accurately preserves boundary integrity and generates clear depth transitions, which can be attributed to the mutual boosting mechanism between depth and

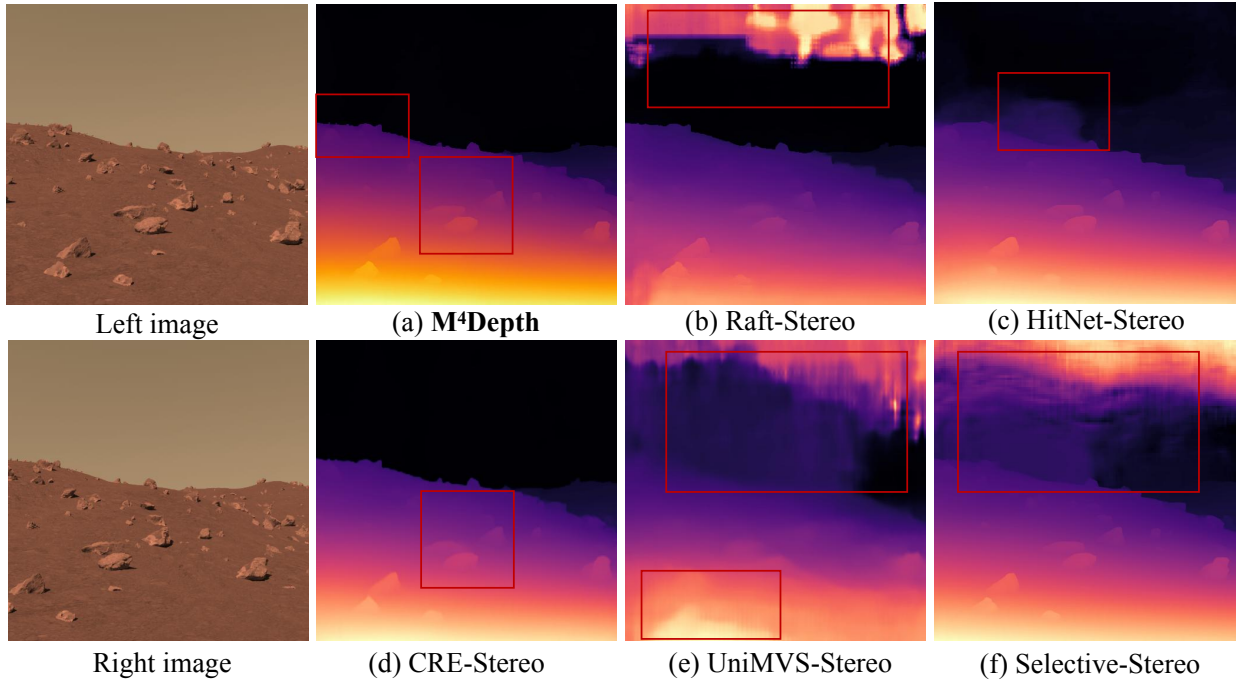


Fig. 11. Qualitative depth prediction results on the SimMars6K dataset. The red boxes highlight the regions to emphasize.

surface normal predictions.

- *Anti-Artifacts.* UniMVS-Stereo *et.al.* introduce significant artifacts and structural distortions, especially in areas with limited visual cues. These artifacts disrupt the geometric continuity of the predicted depth maps. Our method effectively suppresses such artifacts, producing consistent and realistic depth estimations across the scene.

To further demonstrate the applicability of our proposed method in real Martian scenarios, we evaluate M<sup>3</sup>Depth on the Zhurong dataset, which consists of challenging terrain captured by the Zhurong Rover. As illustrated in Fig. 12, our method significantly outperforms previous state-of-the-art approaches across all samples, achieving superior depth estimation quality under complex real-world conditions.

Specifically, M<sup>3</sup>Depth excels in handling texture-less surfaces and maintaining geometric consistency, whereas competing methods often fail in smooth and low-texture areas, such as the flat terrain in the second row, most baseline methods suffer from noisy or inconsistent depth predictions. In contrast, our method produces smooth and coherent depth maps, effectively capturing the terrain’s gradual variations. Our method accurately delineates sharp structures, such as the rover’s components in the first and third rows, where other approaches struggle with boundary artifacts and depth discontinuities. For example, Raft-Stereo and Selective-Stereo introduce noticeable depth bleeding near the rover body and antenna. CRE-Stereo and HitNet-Stereo display significant artifacts in areas with varying lighting or occlusions, which is evident in the regions near the rover structures. However, our model remains robust, preserving the integrity of both depth smoothness and fine-grained details.

These results highlight the ability of M<sup>3</sup>Depth to generalize well to real-world Martian imagery, overcoming chal-

lenges such as flat terrains, texture variations, and occlusions. The superior performance can be attributed to the wavelet-transformed convolutional kernels, which effectively capture multi-frequency features, especially low-frequency components, and the mutual boosting mechanism between depth and surface normals, enhancing overall geometric accuracy.

3) *Ablation Studies:* To assess the impact of each key component in our M<sup>3</sup>Depth framework, we conducted ablation experiments. In Table IV, ✓ indicates the inclusion of the component, while ✗ indicates its absence. The two components evaluated include:

- Wavelet-Enhanced Feature Extractor (WEFE): enhances the feature extraction process via wavelet transform, which is effective for the multi-frequency response, particularly in low-frequency components.
- Iterative Refinement Module (IRM): iteratively refines both depth and surface normal predictions through a mutual boosting mechanism, improving pixel-level depth and surface normal accuracy.

TABLE IV  
ABLATION STUDY OF OUR PROPOSED METHOD ON THE DEPTH PREDICTION EVALUATION.

Setup	WEFE	IRM	Abs Rel (↓)	Sq Rel (↓)	RMSE (↓)	log <sub>10</sub> (↓)	$\delta_1 < 1.25$ (↑)
(a)	✗	✗	0.121	0.083	0.562	0.055	0.825
(b)	✗	✓	0.115	0.071	0.462	0.051	0.871
(c)	✓	✗	0.113	0.066	0.418	0.049	0.882
(d)	✓	✓	0.089	0.058	0.314	0.038	0.905

As summarized in Table IV, the ablation study highlights the contributions of the WEFE and IRM module to the overall performance of our proposed M<sup>3</sup>Depth model. The

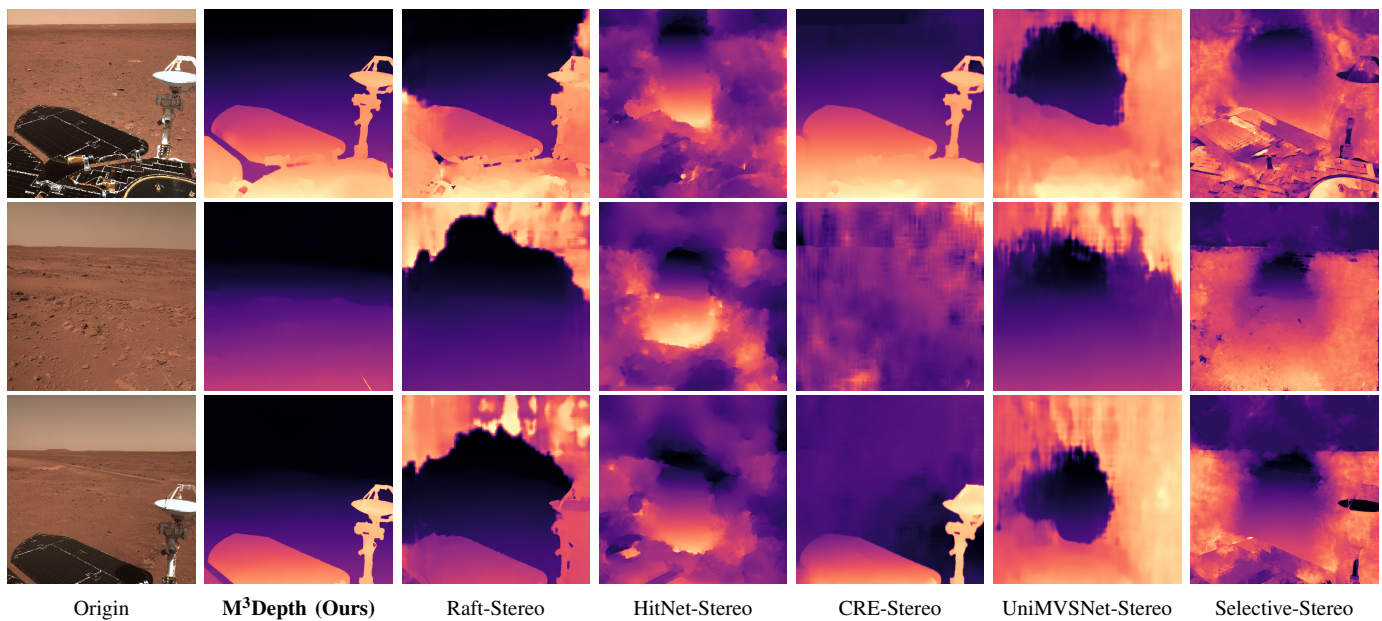


Fig. 12. Qualitative evaluation of depth prediction results on Zhurong Rover images, which demonstrates the generalization ability of our method to real-world Martian image data.

baseline model with both modules absence, *i.e.* Setup (a), performs the worst, with an Abs Rel of 0.121 and RMSE of 0.562, indicating its limited ability to handle Martian terrain challenges. Setup (b) enables only the IRM, achieving an Abs Rel of 0.115 and an RMSE of 0.462. The IRM progressively refines depth predictions, correcting local inconsistencies and enhancing fine-grained details through mutual boosting between depth and surface normal maps. This iterative process is particularly beneficial in handling depth discontinuities and boundary preservation. Similarly, Setup (c) introduces WEFE alone, which reduces Abs Rel to 0.113 and RMSE to 0.418, demonstrating its effectiveness in enhancing feature extraction for texture-less surfaces and boundary regions.

The full model Setup (d) combines WEFE and IRM simultaneously, achieving the best performance, with an Abs Rel of 0.089 and an RMSE of 0.311. The accuracy at  $\delta < 1.25$  also reaches 90.5%, highlighting the complementary roles of WEFE and IRM in achieving accurate and robust depth estimation. WEFE provides a robust feature foundation by capturing both high-frequency and low-frequency details, while IRM iteratively refines these predictions to achieve superior accuracy and consistency.

To further evaluate the individual contributions of the key components in our proposed framework, we conduct an ablation study on surface normal estimation. The results of the ablation study for surface normal estimation, as presented in Table V, further demonstrate the respective contributions of the WEFE and the IRM to our model.

The addition of WEFE leads to a substantial improvement in performance, with the Mean Error reduced to  $25.3^\circ$ , the Median Error decreased to  $17.2^\circ$ , and the RMSE decreased to  $40.7^\circ$ . Furthermore, the  $11.25^\circ$  accuracy increases significantly to 36.1%. This highlights the importance of an enhanced feature extraction strategy, emphasizing that low-

frequency signals are also essential for accurate surface normal estimation. On the other hand, the IRM module demonstrates a more pronounced impact on depth estimation than surface normal estimation. This is mainly because surface normals inherently rely on local gradients, which are less affected by iterative refinements.

TABLE V  
ABLATION STUDY OF OUR PROPOSED METHOD ON THE SURFACE NORMAL MAP PREDICTION EVALUATION.

Setup	WEFE	IRM	Mean ( $\downarrow$ )	Median ( $\downarrow$ )	RMSE <sub>n</sub> ( $\downarrow$ )	$11.25^\circ$ ( $\uparrow$ )
(a)	✗	✗	33.5	24.2	50.9	0.179
(b)	✗	✓	29.6	20.8	46.9	0.275
(c)	✓	✗	25.3	17.2	40.7	0.361
(d)	✓	✓	20.6	12.3	34.2	0.435

To provide a more intuitive understanding of the contribution of each module in our proposed method, we visualize the depth estimation results under different ablation settings, as shown in Fig. 13. From the results, it is evident that the baseline model Setup (a), which lacks both WEFE and IRM, produces depth maps with evident artifacts, particularly in texture-less regions and at object boundaries. In Setup (b), it shows sharper boundaries. However, this model struggles with texture-less regions and exhibits poor depth continuity. In Setup (c), solely introducing WEFE results in a notable improvement, which demonstrates smoother depth transitions and reduced artifacts. However, due to the absence of the surface normal as an auxiliary geometric information, the model tends to over smooth object boundaries, such as the edges of rocks.



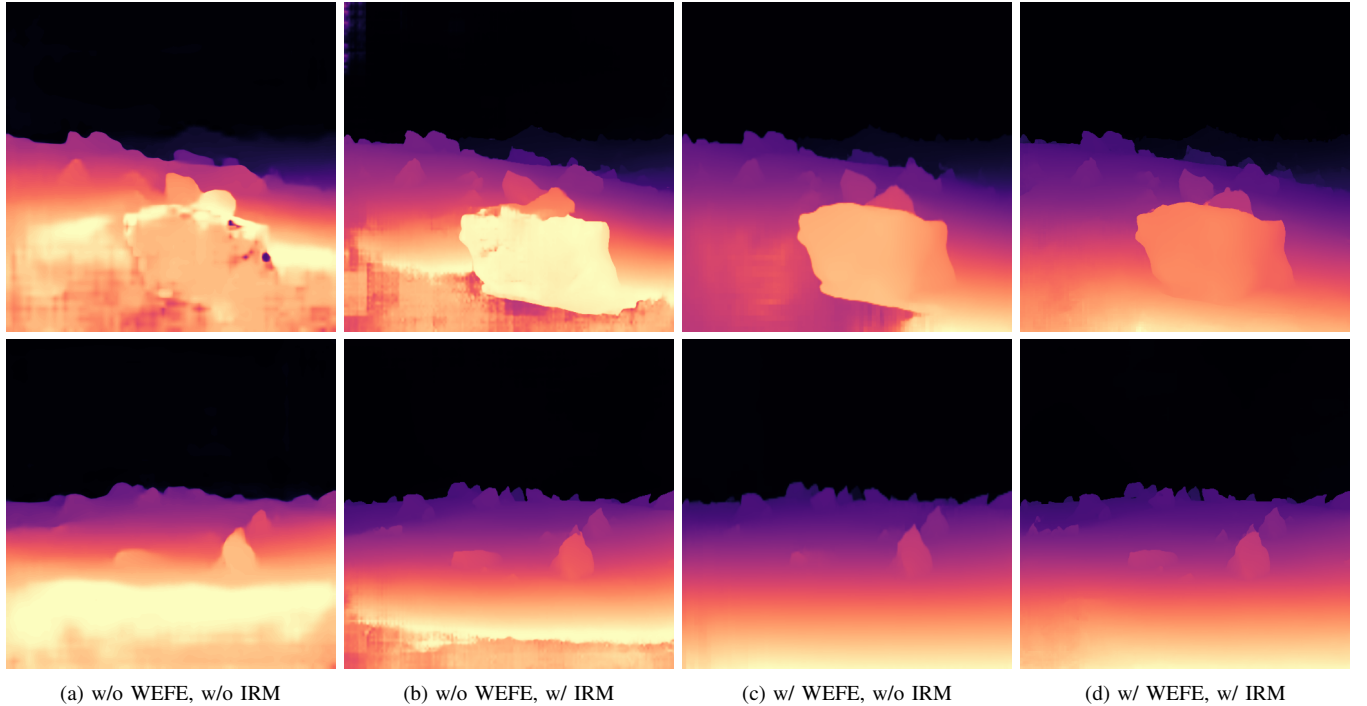


Fig. 13. Ablation study visualization results. Comparison of depth estimation results under different ablation settings. w/ means “with”, w/o means “without”.

### C. Further Applications and Future Works

While our proposed framework demonstrates significant improvements in depth estimation for Martian terrains, certain aspects deserve further exploration to broaden the applicability and address future works.

**Further Applications.** (a) 3D Scene Perception for Mars Rovers: The capability to generate high-resolution 3D reconstructions makes our framework a promising tool for enhancing the perception systems of Mars rovers. By improving 3D scene understanding, the framework can facilitate more efficient navigation, obstacle avoidance, and scientific exploration in unstructured Martian environments. (b) Depth Completion for Sparse Depth Data: Current Martian datasets, such as those provided by NASA, often include sparse ground truth depth maps with limited density, making it challenging to generate complete and detailed 3D models. Given the intrinsic relationship between surface normals and depth, it is feasible to leverage the more easily estimated surface normals to fill in missing depth values, which may bridge the gap in sparse datasets and make them more usable for comprehensive 3D modeling.

**Future Works.** (a) Despite its strong performance in synthetic datasets, our model still has room for improvement when applied to real-world data from the Zhurong Rover, which operates in the relatively flat Utopia Planitia region. This area is characterized by smooth terrains and low-frequency variations, making it challenging to capture fine-grained details. While our framework mitigates some of these issues by amplifying low-frequency signals, reconstructing intricate surface features requires further research. Addressing this challenge may require developing novel strategies tailored to homogeneous and texture-less environments, such as integrating more advanced

priors or domain-specific features. (b) Semantic information, such as identifying rocks, sand, or craters, could enhance depth estimation by providing contextual cues. However, incorporating semantic priors introduces computational overhead and often necessitates redesigning the network for joint learning, complicating the training process. Moreover, in regions with flat terrains or sparse visual features, semantic information may lack sufficient resolution to offer meaningful guidance, thereby limiting its effectiveness in improving the depth estimation results. We hope this work can provide a hope beyond the shadow of a dream, contributing a little to unlocking new possibilities in planetary exploration and scientific discovery.

## VI. CONCLUSION

In this paper, we proposed M<sup>3</sup>Depth, a depth estimation model specifically designed for Mars rovers to address the challenges posed by the sparse and unstructured terrain on Mars. Our approach focused on tackling two critical issues, the dominance of low-frequency features in Martian imagery and the lack of explicit geometric constraints. To address the former, we incorporated a wavelet-enhanced convolutional kernel. It is capable of capturing more low-frequency components and effectively expanding the receptive field. To overcome the latter, we introduced a consistency loss that explicitly modeled the geometric complementary relationship between depth maps and surface normal maps. By leveraging surface normal as an auxiliary modal to enhance depth estimation accuracy. Additionally, we developed an iterative refinement module with a mutual boosting mechanism that jointly enhance both depth and surface normal predictions in a complementary manner. Finally, we validated the effectiveness of M<sup>3</sup>Depth on SimMar6k dataset with ground-truth depth

labels and further evaluated in real-world Martian scenarios. Experimental results demonstrated that our method significantly outperformed SoTA approaches across multiple metrics, showcasing its accuracy and adaptability to challenging real Martian environments.

#### ACKNOWLEDGMENTS

We thank the release of the awesome dataset SimMars6K that makes this study possible. We also acknowledge China's Mars Mission Program for supplying the Tianwen-1 image data. The Tianwen-1 datasets used in this paper are processed and produced by Ground Research and Application System of China's Lunar and Planetary Exploration Program. These dataset are available for application and downloaded at <http://moon.bao.ac.cn/>. Additionally, we sincerely thank all anonymous reviewers and editors for their insightful comments and helpful suggestions.

#### REFERENCES

- [1] J. Strader, K. Otsu, and A.-a. Agha-mohammadi, "Perception-aware autonomous mast motion planning for planetary exploration rovers," *Journal of Field Robotics*, vol. 37, no. 5, pp. 812–829, 2020.
- [2] A. Rankin, M. Maimone, J. Biesiadecki, N. Patel, D. Levine, and O. Toupet, "Driving curiosity: Mars rover mobility trends during the first seven years," in *2020 IEEE Aerospace Conference*. IEEE, 2020, pp. 1–19.
- [3] T. Zhang, S. Peng, Y. Jia, H. Tian, J. Sun, and C. Yan, "Slip estimation for mars rover zhurong based on data drive," *Applied Sciences*, vol. 12, no. 3, p. 1676, 2022.
- [4] W. Yin, C. Zhang, H. Chen, Z. Cai, G. Yu, K. Wang, X. Chen, and C. Shen, "Metric3d: Towards zero-shot metric 3d prediction from a single image," in *Proceedings of the IEEE/CVF International Conference on Computer Vision*, 2023, pp. 9043–9053.
- [5] T. Panambur, D. Chakraborty, M. Meyer, R. Milliken, E. Learned-Miller, and M. Parente, "Self-supervised learning to guide scientifically relevant categorization of martian terrain images," in *Proceedings of the IEEE/CVF Conference on Computer Vision and Pattern Recognition*, 2022, pp. 1322–1332.
- [6] P. Tian, M. Yao, X. Xiao, B. Zheng, T. Cao, Y. Xi, H. Liu, and H. Cui, "3-d semantic terrain reconstruction of monocular close-up images of martian terrains," *IEEE Transactions on Geoscience and Remote Sensing*, vol. 62, pp. 1–16, 2024.
- [7] D. Shim and H. J. Kim, "Swindepth: Unsupervised depth estimation using monocular sequences via swin transformer and densely cascaded network," in *2023 IEEE International Conference on Robotics and Automation (ICRA)*. IEEE, 2023, pp. 4983–4990.
- [8] R. M. Swan, D. Atha, H. A. Leopold, M. Gildner, S. Oij, C. Chiu, and M. Ono, "Ai4mars: A dataset for terrain-aware autonomous driving on mars," in *Proceedings of the IEEE/CVF conference on computer vision and pattern recognition*, 2021, pp. 1982–1991.
- [9] Y. Xiong, X. Xiao, M. Yao, H. Cui, and Y. Fu, "Light4mars: A lightweight transformer model for semantic segmentation on unstructured environment like mars," *ISPRS Journal of Photogrammetry and Remote Sensing*, vol. 214, pp. 167–178, 2024.
- [10] C. Ma, Y. Li, J. Lv, Z. Xiao, W. Zhang, and L. Mo, "Automated rock detection from mars rover image via y-shape dual-task network with depth-aware spatial attention mechanism," *IEEE Transactions on Geoscience and Remote Sensing*, 2024.
- [11] J. Liu, C. Li, R. Zhang, W. Rao, X. Cui, Y. Geng, Y. Jia, H. Huang, X. Ren, W. Yan *et al.*, "Geomorphic contexts and science focus of the zhurong landing site on mars," *Nature Astronomy*, vol. 6, no. 1, pp. 65–71, 2022.
- [12] J. Bell, J. Maki, G. Mehall, M. Ravine, M. Caplinger, Z. Bailey, S. Brylow, J. Schaffner, K. Kinch, M. Madsen *et al.*, "The mars 2020 perseverance rover mast camera zoom (mascam-z) multispectral, stereoscopic imaging investigation," *Space science reviews*, vol. 217, pp. 1–40, 2021.
- [13] H. Liu, M. Yao, X. Xiao, and H. Cui, "A hybrid attention semantic segmentation network for unstructured terrain on mars," *Acta Astronautica*, vol. 204, pp. 492–499, 2023.
- [14] J. Li, W. Lv, J. Wang, Y. Wang, and Y. Liu, "Unsupervised denoising with implicit noise mapping for single martian multispectral image," in *IGARSS 2024-2024 IEEE International Geoscience and Remote Sensing Symposium*. IEEE, 2024, pp. 6120–6123.
- [15] M. Li, J. Li, Y. Wang, Y. Liu, and H. Xu, "Dustnet: An unsupervised and noise-resistant network for martian dust storm change detection," *IEEE Geoscience and Remote Sensing Letters*, 2025.
- [16] S. E. Finder, R. Amoyal, E. Treister, and O. Freifeld, "Wavelet convolutions for large receptive fields," in *European Conference on Computer Vision*. Springer, 2025, pp. 363–380.
- [17] P. Gavrikov and J. Keuper, "Can biases in imagenet models explain generalization?" in *Proceedings of the IEEE/CVF Conference on Computer Vision and Pattern Recognition*, 2024, pp. 22 184–22 194.
- [18] Q. Yang, L. Wang, R. Yang, H. Stewenius, and D. Nistér, "Stereo matching with color-weighted correlation, hierarchical belief propagation, and occlusion handling," *IEEE transactions on pattern analysis and machine intelligence*, vol. 31, no. 3, pp. 492–504, 2008.
- [19] E. Tola, V. Lepetit, and P. Fua, "Daisy: An efficient dense descriptor applied to wide-baseline stereo," *IEEE transactions on pattern analysis and machine intelligence*, vol. 32, no. 5, pp. 815–830, 2009.
- [20] Z. Rao, X. Li, B. Xiong, Y. Dai, Z. Shen, H. Li, and Y. Lou, "Cascaded recurrent networks with masked representation learning for stereo matching of high-resolution satellite images," *ISPRS Journal of Photogrammetry and Remote Sensing*, vol. 218, pp. 151–165, 2024.
- [21] W. Luo, A. G. Schwing, and R. Urtasun, "Efficient deep learning for stereo matching," in *Proceedings of the IEEE conference on computer vision and pattern recognition*, 2016, pp. 5695–5703.
- [22] J. Žbontar and Y. LeCun, "Stereo matching by training a convolutional neural network to compare image patches," *Journal of Machine Learning Research*, vol. 17, no. 65, pp. 1–32, 2016.
- [23] Z. Li, X. Liu, N. Drenkow, A. Ding, F. X. Creighton, R. H. Taylor, and M. Unberath, "Revisiting stereo depth estimation from a sequence-to-sequence perspective with transformers," in *Proceedings of the IEEE/CVF international conference on computer vision*, 2021, pp. 6197–6206.
- [24] B. Huang, J.-Q. Zheng, S. Giannarou, and D. S. Elson, "H-net: Unsupervised attention-based stereo depth estimation leveraging epipolar geometry," in *Proceedings of the IEEE/CVF Conference on Computer Vision and Pattern Recognition*, 2022, pp. 4460–4467.
- [25] W. Chuah, R. Tennakoon, R. Hoseinnezhad, and A. Bab-Hadiashar, "Deep learning-based incorporation of planar constraints for robust stereo depth estimation in autonomous vehicle applications," *IEEE Transactions on Intelligent Transportation Systems*, vol. 23, no. 7, pp. 6654–6665, 2021.
- [26] H. Yan, S. Zhang, Y. Zhang, and L. Zhang, "Monocular depth estimation with guidance of surface normal map," *Neurocomputing*, vol. 280, pp. 86–100, 2018.
- [27] T. L. da Silveira, P. G. Pinto, J. Murrugarra-Llerena, and C. R. Jung, "3d scene geometry estimation from 360 imagery: A survey," *ACM Computing Surveys*, vol. 55, no. 4, pp. 1–39, 2022.
- [28] U. Kusupati, S. Cheng, R. Chen, and H. Su, "Normal assisted stereo depth estimation," in *Proceedings of the IEEE/CVF conference on computer vision and pattern recognition*, 2020, pp. 2189–2199.
- [29] J. Zhang, L. Lin, Z. Fan, W. Wang, and J. Liu, "S5mars: Semi-supervised learning for mars semantic segmentation," *IEEE Transactions on Geoscience and Remote Sensing*, vol. 62, p. 3386756, 2024.
- [30] W. Lv, L. Wei, D. Zheng, Y. Liu, and Y. Wang, "Marsnet: Automated rock segmentation with transformers for tianwen-1 mission," *IEEE Geoscience and Remote Sensing Letters*, vol. 20, pp. 1–5, 2022.
- [31] D. Zheng, L. Wei, W. Lv, Y. Liu, and Y. Wang, "Rover attitude and camera parameter: Rock measurements on mars surface based on rover attitude and camera parameter for tianwen-1 mission," *Remote Sensing*, vol. 15, no. 18, p. 4388, 2023.
- [32] R. Liu, Y. Xu, and Q. Yang, "High-resolution and spatial-continuous 3d model reconstruction of martian surface by integrating multi-sensor data of zhurong rover," *IEEE Transactions on Geoscience and Remote Sensing*, 2024.
- [33] K.-J. Yoon and I. S. Kweon, "Adaptive support-weight approach for correspondence search," *IEEE transactions on pattern analysis and machine intelligence*, vol. 28, no. 4, pp. 650–656, 2006.
- [34] A. Hosni, C. Rhemann, M. Bleyer, C. Rother, and M. Gelautz, "Fast cost-volume filtering for visual correspondence and beyond," *IEEE transactions on pattern analysis and machine intelligence*, vol. 35, no. 2, pp. 504–511, 2012.
- [35] H. Xu and J. Zhang, "Aanet: Adaptive aggregation network for efficient stereo matching," in *Proceedings of the IEEE/CVF conference on computer vision and pattern recognition*, 2020, pp. 1959–1968.

- [36] F. Zhang, V. Prisacariu, R. Yang, and P. H. Torr, "Ga-net: Guided aggregation net for end-to-end stereo matching," in *Proceedings of the IEEE/CVF conference on computer vision and pattern recognition*, 2019, pp. 185–194.
- [37] A. Pilzer, S. Lathuilière, D. Xu, M. M. Puscas, E. Ricci, and N. Sebe, "Progressive fusion for unsupervised binocular depth estimation using cycled networks," *IEEE transactions on pattern analysis and machine intelligence*, vol. 42, no. 10, pp. 2380–2395, 2019.
- [38] M. Ji, J. Gall, H. Zheng, Y. Liu, and L. Fang, "Surfacenet: An end-to-end 3d neural network for multiview stereopsis," in *Proceedings of the IEEE international conference on computer vision*, 2017, pp. 2307–2315.
- [39] S. Khamis, S. Fanello, C. Rhemann, A. Kowdle, J. Valentin, and S. Izadi, "Stereonet: Guided hierarchical refinement for real-time edge-aware depth prediction," in *Proceedings of the European conference on computer vision (ECCV)*, 2018, pp. 573–590.
- [40] X. Cheng, Y. Zhong, M. Harandi, Y. Dai, X. Chang, H. Li, T. Drummond, and Z. Ge, "Hierarchical neural architecture search for deep stereo matching," *Advances in neural information processing systems*, vol. 33, pp. 22 158–22 169, 2020.
- [41] H. Laga, L. V. Jospin, F. Boussaid, and M. Bennamoun, "A survey on deep learning techniques for stereo-based depth estimation," *IEEE Transactions on Pattern Analysis and Machine Intelligence*, vol. 44, no. 4, pp. 1738–1764, 2022.
- [42] F. Güney and A. Geiger, "Displets: Resolving stereo ambiguities using object knowledge," in *Proceedings of the IEEE conference on computer vision and pattern recognition*, 2015, pp. 4165–4175.
- [43] A. Kendall, H. Martirosyan, S. Dasgupta, P. Henry, R. Kennedy, A. Bachrach, and A. Bry, "End-to-end learning of geometry and context for deep stereo regression," in *Proceedings of the IEEE international conference on computer vision*, 2017, pp. 66–75.
- [44] A. Shaked and L. Wolf, "Improved stereo matching with constant highway networks and reflective confidence learning," in *Proceedings of the IEEE conference on computer vision and pattern recognition*, 2017, pp. 4641–4650.
- [45] W. Yin, Y. Liu, C. Shen, and Y. Yan, "Enforcing geometric constraints of virtual normal for depth prediction," in *Proceedings of the IEEE/CVF international conference on computer vision*, 2019, pp. 5684–5693.
- [46] M. Gui, J. S. Fischer, U. Prestel, P. Ma, D. Kotovenko, O. Grebenkova, S. A. Baumann, V. T. Hu, and B. Ommer, "Depthfm: Fast monocular depth estimation with flow matching," *arXiv preprint arXiv:2403.13788*, 2024.
- [47] G. Bae, I. Budvytis, and R. Cipolla, "Irondepth: Iterative refinement of single-view depth using surface normal and its uncertainty," *arXiv preprint arXiv:2210.03676*, 2022.
- [48] S. Shao, Z. Pei, W. Chen, X. Wu, and Z. Li, "Nddepth: Normal-distance assisted monocular depth estimation," in *Proceedings of the IEEE/CVF International Conference on Computer Vision*, 2023, pp. 7931–7940.
- [49] X. Xiao, M. Yao, H. Liu, J. Wang, L. Zhang, and Y. Fu, "A kernel-based multi-featured rock modeling and detection framework for a mars rover," *IEEE Transactions on Neural Networks and Learning Systems*, vol. 34, no. 7, pp. 3335–3344, 2021.
- [50] X. Wang, G. Xu, H. Jia, and X. Yang, "Selective-stereo: Adaptive frequency information selection for stereo matching," in *Proceedings of the IEEE/CVF Conference on Computer Vision and Pattern Recognition*, 2024, pp. 19 701–19 710.
- [51] H. Zhao, H. Zhou, Y. Zhang, J. Chen, Y. Yang, and Y. Zhao, "High-frequency stereo matching network," in *Proceedings of the IEEE/CVF conference on computer vision and pattern recognition*, 2023, pp. 1327–1336.
- [52] H. Hirschmüller, "Stereo processing by semiglobal matching and mutual information," *IEEE Transactions on pattern analysis and machine intelligence*, vol. 30, no. 2, pp. 328–341, 2007.
- [53] D. Scharstein and R. Szeliski, "A taxonomy and evaluation of dense two-frame stereo correspondence algorithms," *International journal of computer vision*, vol. 47, pp. 7–42, 2002.
- [54] Y. Zhan, Y. Gu, K. Huang, C. Zhang, and K. Hu, "Accurate image-guided stereo matching with efficient matching cost and disparity refinement," *IEEE Transactions on Circuits and Systems for Video Technology*, vol. 26, no. 9, pp. 1632–1645, 2015.
- [55] N. Kaur, N. Nazir *et al.*, "A review of local binary pattern based texture feature extraction," in *2021 9th International Conference on Reliability, Infocom Technologies and Optimization (Trends and Future Directions)(ICRITO)*. IEEE, 2021, pp. 1–4.
- [56] X. Qi, R. Liao, Z. Liu, R. Urtasun, and J. Jia, "Geonet: Geometric neural network for joint depth and surface normal estimation," in *Proceedings of the IEEE Conference on Computer Vision and Pattern Recognition*, 2018, pp. 283–291.
- [57] Z. Ji, X. Song, H. Song, H. Yang, and X. Guo, "Rdrf-net: A pyramid architecture network with residual-based dynamic receptive fields for unsupervised depth estimation," *Neurocomputing*, vol. 457, pp. 1–12, 2021.
- [58] W. Guo, G. Xu, B. Liu, and Y. Wang, "Hyperspectral image classification using cnn-enhanced multi-level haar wavelet features fusion network," *IEEE Geoscience and Remote Sensing Letters*, vol. 19, pp. 1–5, 2022.
- [59] J.-J. Huang and P. L. Dragotti, "Winnet: Wavelet-inspired invertible network for image denoising," *IEEE Transactions on Image Processing*, vol. 31, pp. 4377–4392, 2022.
- [60] G. Bae and A. J. Davison, "Rethinking inductive biases for surface normal estimation," in *Proceedings of the IEEE/CVF Conference on Computer Vision and Pattern Recognition*, 2024, pp. 9535–9545.
- [61] L. Lipson, Z. Teed, and J. Deng, "Raft-stereo: Multilevel recurrent field transforms for stereo matching," in *2021 International Conference on 3D Vision (3DV)*. IEEE, 2021, pp. 218–227.
- [62] X. Zeng, J. Liu, X. Ren, W. Yan, Q. Fu, X. Gao, W. Chen, W. Zuo, and C. Li, "Pan-location mapping and localization for the in-situ science exploration of zhurong mars rover," *Science China Information Sciences*, vol. 65, no. 7, p. 172201, 2022.
- [63] D. F. Fouhey, A. Gupta, and M. Hebert, "Data-driven 3d primitives for single image understanding," in *Proceedings of the IEEE International Conference on Computer Vision*, 2013, pp. 3392–3399.
- [64] V. Tankovich, C. Hane, Y. Zhang, A. Kowdle, S. Fanello, and S. Bouaziz, "Hitnet: Hierarchical iterative tile refinement network for real-time stereo matching," in *Proceedings of the IEEE/CVF Conference on Computer Vision and Pattern Recognition*, 2021, pp. 14 362–14 372.
- [65] J. Li, P. Wang, P. Xiong, T. Cai, Z. Yan, L. Yang, J. Liu, H. Fan, and S. Liu, "Practical stereo matching via cascaded recurrent network with adaptive correlation," in *Proceedings of the IEEE/CVF conference on computer vision and pattern recognition*, 2022, pp. 16 263–16 272.
- [66] R. Peng, R. Wang, Z. Wang, Y. Lai, and R. Wang, "Rethinking depth estimation for multi-view stereo: A unified representation," in *Proceedings of the IEEE/CVF conference on computer vision and pattern recognition*, 2022, pp. 8645–8654.
- [67] J. Zeng, Y. Tong, Y. Huang, Q. Yan, W. Sun, J. Chen, and Y. Wang, "Deep surface normal estimation with hierarchical rgb-d fusion," in *Proceedings of the IEEE/CVF conference on computer vision and pattern recognition*, 2019, pp. 6153–6162.



**Junjie Li** (Student Member, IEEE) received the B.S. degree in 2022 from Beijing University of Posts and Telecommunications, China. He is currently pursuing his Ph.D. degree in Beijing University of Posts and Telecommunications, China. His research interests include wireless multimedia transmission and Mars scene perception. Email: junjie@bupt.edu.cn



**Jiawei Wang** (Student Member, IEEE) received the B.S. and Master degree from Beijing University of Posts and Telecommunications in 2020 and 2023, respectively. He is currently working toward the Ph.D. degree in State Key Laboratory of Networking and Switching Technology, Beijing University of Posts and Telecommunications. His research interests include Computer Vision and Embodied Artificial Intelligence.



**Miyu Li** received the B.S. degree in 2024 from Beijing University of Posts and Telecommunications, China. She is currently pursuing his master degree in Beijing University of Posts and Telecommunications, China. Her research interests include change detection and terrain classification. Email: limy\_bupt@foxmail.com



**Yu Liu** (Member, IEEE) received her B.S. degree in automatic control and Ph.D. degree in signal and information processing in 2001 and 2006 respectively, both from Beijing University of Posts and Telecommunications, China. Dr. Liu is currently an associate professor and a doctoral supervisor with Beijing University of Posts and Telecommunications, China. Her main research areas include compressive sensing, blockchain security, and Mars images processing. Email: liuy@bupt.edu.cn



**Yumei Wang** (Member, IEEE) received the Ph.D. degree in Signal and Information Processing from Beijing University of Posts and Telecommunications in 2004. She worked as an intern researcher in YRP center of NTT DoCoMo, Japan, in the summer of 2001. From April 2011 to April 2012, she was working as a visiting scholar in Lehigh University, USA. Currently she is an associate professor in Beijing University of Posts and Telecommunications. Her research interests include multimedia signal processing, cross-layer design for wireless multimedia

transmission, and distributed video coding. Email: ymwang@bupt.edu.cn



**Haitao Xu** received the B.E. and M.S. degrees in electrical engineering from Beijing Jiaotong University, Beijing, China, in 2005 and 2008, respectively. He received the Ph.D. degree in computer application technology with the University of Chinese Academy of Sciences, Beijing, in 2024, under the supervision of Dr. Changbin Xue.

He is currently a Professor and a Master's Supervisor with the Key Laboratory of Electronics Information Technology for Complex Space Systems, National Space Science Center, Chinese Academy of Sciences, Beijing. His research interests include aerospace-integrated electronic system technology and space-intelligent information processing technology. Email: xuhaitao@nssc.ac.cn



## APPENDIX A

## CONSISTENCY CONSTRAINTS FORMULATION BETWEEN DEPTH AND SURFACE NORMAL

Under the pinhole camera model, the spatial gradient of the depth map in the pixel coordinate system is computed by integrating information from both the depth and surface normal maps. As illustrated in Fig. 14,  $(u, v)$  represents the pixel coordinate corresponding to the 3D point  $(X, Y, Z)$ , and  $(u_c, v_c)$  denotes the pixel coordinate of the camera's optical center. Additionally,  $f_x$  and  $f_y$  represent the focal lengths along the X-axis and Y-axis, respectively.

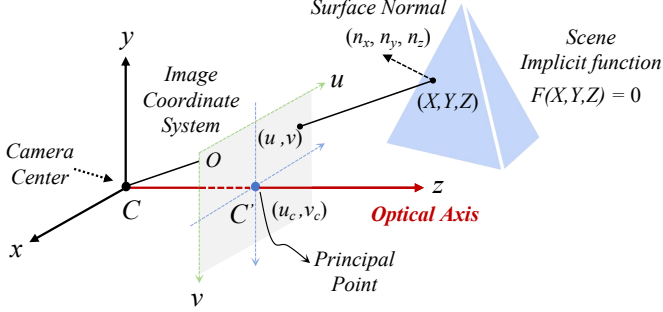


Fig. 14. Pinhole camera model and the scene implicit function.

Based on fundamental principles of photogrammetry, the pixel coordinates  $(u, v)$  can be transformed into three-dimensional spatial coordinates  $(X, Y, Z)$ , as Eq.(32) depicts.

$$\begin{bmatrix} u \\ v \\ 1 \end{bmatrix} = \frac{1}{Z} \begin{bmatrix} f_x & 0 & u_c \\ 0 & f_y & v_c \\ 0 & 0 & 1 \end{bmatrix} \begin{bmatrix} X \\ Y \\ Z \end{bmatrix}. \quad (32)$$

Based on the pinhole camera model and the chain rule, we can yield equation below:

$$\begin{aligned} X &= \frac{Z(u - u_c)}{f_x} \Rightarrow \frac{\partial X}{\partial u} = \frac{u - u_c}{f_x} \frac{\partial Z}{\partial u} + \frac{Z}{f_x}, \\ Y &= \frac{Z(v - v_c)}{f_y} \Rightarrow \frac{\partial Y}{\partial u} = \frac{v - v_c}{f_y} \frac{\partial Z}{\partial u}. \end{aligned} \quad (33)$$

Likewise, we can obtain the following equation:

$$\begin{cases} \frac{\partial X}{\partial v} = \frac{u - u_c}{f_x} \frac{\partial Z}{\partial v}, \\ \frac{\partial Y}{\partial v} = \frac{v - v_c}{f_y} \frac{\partial Z}{\partial v} + \frac{Z}{f_y}. \end{cases} \quad (34)$$

Depth and surface normal information are inherently related through the geometry of the 3D scene. To ensure consistency between these two modalities, we consider two types of constraints as follows.

#### Constraints 1: Geometric Mathematical Constraint.

The first constraint is derived from the mathematical relationship between depth gradients and surface normals. The surface normal can be expressed as the gradient of an implicit function, and this relationship provides a direct linkage between depth gradients and normal vectors.

Under the surface function assumption, the scene can be represented as an implicit function  $F(X, Y, Z) = 0$ . The

surface normal map, denoted as  $\vec{n} = (n_x, n_y, n_z)$ , can be interpreted as the gradient of this function:

$$\nabla F = \left( \frac{\partial F}{\partial X}, \frac{\partial F}{\partial Y}, \frac{\partial F}{\partial Z} \right) = (n_x, n_y, n_z). \quad (35)$$

Then, by taking the partial derivatives of  $F(X, Y, Z) = 0$  with respect to  $X$  and  $Y$ , we can derive:

$$\begin{cases} \frac{\partial F}{\partial X} + \frac{\partial F}{\partial Z} \frac{\partial Z}{\partial X} = 0 \Rightarrow \frac{\partial Z}{\partial X} = -\frac{\frac{\partial F}{\partial X}}{\frac{\partial F}{\partial Z}} = -\frac{n_x}{n_z}, \\ \frac{\partial F}{\partial Y} + \frac{\partial F}{\partial Z} \frac{\partial Z}{\partial Y} = 0 \Rightarrow \frac{\partial Z}{\partial Y} = -\frac{\frac{\partial F}{\partial Y}}{\frac{\partial F}{\partial Z}} = -\frac{n_y}{n_z}. \end{cases} \quad (36)$$

By integrating from Eq.(33) to Eq.(36), we can derive the depth gradient in the pixel coordinate space  $(u, v)$  as follows:

$$\begin{cases} \left( \frac{\partial Z}{\partial u} \right)_1 = \frac{\partial Z}{\partial X} \frac{\partial X}{\partial u} + \frac{\partial Z}{\partial Y} \frac{\partial Y}{\partial u}, \\ \left( 1 + \frac{n_x}{n_z} \frac{u - u_c}{f_x} + \frac{n_y}{n_z} \frac{v - v_c}{f_y} \right) \frac{\partial Z}{\partial u} = -\frac{n_x Z}{n_z f_x}, \\ \left( \frac{\partial Z}{\partial u} \right)_1 = \frac{\left( -\frac{n_x Z}{n_z f_x} \right)}{1 + \frac{n_x}{n_z} \frac{u - u_c}{f_x} + \frac{n_y}{n_z} \frac{v - v_c}{f_y}}. \end{cases} \quad (37)$$

Similarly, we can yield equation below:

$$\left( \frac{\partial Z}{\partial v} \right)_1 = \frac{\left( -\frac{n_y Z}{n_z f_y} \right)}{1 + \frac{n_x}{n_z} \frac{u - u_c}{f_x} + \frac{n_y}{n_z} \frac{v - v_c}{f_y}} \quad (38)$$

#### Estimate 2: Spatial Gradient Constraint.

The spatial gradient of the depth map can be efficiently estimated using standard image processing techniques, such as the Sobel filter, which approximates local depth variations in the image. This gradient captures changes in depth along the horizontal and vertical directions, providing a data-driven estimate of the surface geometry structure. The spatial gradient of the depth map can be computed by using a Sobel filter:

$$\left( \frac{\partial Z}{\partial u}, \frac{\partial Z}{\partial v} \right)_2 = \left( \frac{\Delta Z}{\Delta u}, \frac{\Delta Z}{\Delta v} \right). \quad (39)$$

The consistency constraint is formulated as deviation between the two constraints of  $\left( \frac{\partial Z}{\partial u}, \frac{\partial Z}{\partial v} \right)_1$  and  $\left( \frac{\partial Z}{\partial u}, \frac{\partial Z}{\partial v} \right)_2$ . The consistency constraint is further formulated as a consistency loss function, enabling it to guide model training by aligning the two gradient estimates. This loss is defined as the Huber norm of their deviation, as shown in Eq.(40).

$$\mathcal{L}_c = \left| \left( \frac{\partial Z}{\partial u}, \frac{\partial Z}{\partial v} \right)_1 - \left( \frac{\partial Z}{\partial u}, \frac{\partial Z}{\partial v} \right)_2 \right|_{\mathbf{H}}. \quad (40)$$